Control System for Dual-Mode Operation of Grid-Tied Photovoltaic and Wind Energy Conversion Systems with Active and Reactive Power Injection

By

Labib

A Thesis Submitted to Saint Mary's University, Halifax, Nova Scotia
in Partial Fulfillment of the Requirements for
the Degree of Master of Science in Applied Science

August 8, 2017, Halifax, Nova Scotia

Copyright Labib, 2017

Approved:	Dr. Adel Merabet Supervisor Division of Engineering
Approved:	Dr. David Swingler Supervisory Committee Member Division of Engineering
Approved:	Dr. A. M. Y. Mohammad Ghias Supervisory Committee Member Assistant Professor University of Sharjah, UAE
Approved:	Dr. Mo El-Hawary External Examiner Professor Dalhousie University, Halifax
Date:	August 8, 2017

Control System for Dual-Mode Operation of Grid-Tied Photovoltaic and Wind Energy Conversion Systems with Active and Reactive Power Injection

By Labib

Abstract

The purpose of the work is to design and implement a dual mode control operation of grid-connected renewable (photovoltaic or wind) energy conversion systems with a low-voltage ride through capability. Control systems for normal and grid fault condition are presented for the generator and grid sides. In normal grid condition, the dc-dc converter is controlled in order to achieve maximum power extraction, and the inverter is controlled to maintain a constant dc-link voltage and power transfer at a unity power factor. In grid fault condition, the dc-link voltage regulation is achieved by the dc-dc converter and the required active and reactive powers injection are achieved by the inverter to meet the grid code requirements. The proposed control system is experimentally validated for the normal and faulty grid condition with three-phase grid-connected photovoltaic and wind energy conversion system using the OPAL-RT and Festo rapid control prototyping system. Experimental results demonstrate the effectiveness and robustness of the proposed system under different working conditions.

August 8, 2017

Acknowledgement

I would like to thank Saint Mary's University for providing me the opportunity to pursue the M. Sc. in Applied Science program with funding and research fellowship. I am also thankful to Canada Foundation of Innovation for the Grant (Grant# 30527), Faculty of Graduate Studies and Research, and Government of Nova Scotia for Nova Scotia Graduate Scholarship. I would like to express my sincere gratitude to my supervisor Dr. Adel Merabet for his diligent guidance, inspiration, and patience all through the research work.

I would like to thank my supervisory committee member Dr. David Swingler and Dr. A. M. Y. Mohammad Ghias for their valuable comments and suggestions to improve the quality of this work. The author also expresses his gratitude to external supervisor Dr. Mo El-Hawary for providing support and carefully reviewing this thesis. Without their guidance and feedback, the thesis work could not have been a success.

I would also like to thank the entire research group of Laboratory of Control Systems and Mechatronics and Division of Engineering at Saint Mary's University for their support and help.

Finally, the author is indebted to his family and friends who have been encouraged and motivated to complete this work. I would like to dedicate the effort done in this thesis to my parents who always pray for me.

August 8, 2017

Table of Contents

List of Figures

List of Tables

Nomenclature

Solar Photovoltaic (PV) Energy Conversion

i_p	PV array current
i_0	Output current of the boost converter
v_0	PV array voltage
L_B	Line inductance of the dc-dc boost converter
C	Capacitance
v_{dc}	Voltage output of the boost converter
R_S	Series resistance of the solar cell
R_{sh}	Shunt resistance of the solar cell
i_{sat}	Diode saturation current
q	Electron charge
n_s	Number of cells in series
n_p	Number of cells in parallel

$P_{\max}$	Maximum power of the PV array
i_{pv}	Photocurrent of the PV cell
I_{RS}	Diode reverse saturation current
I_S	Diode saturation current
K	Boltzmann's Constant
N	Diode Ideality Factor
T	Temperature
$V_{\max}$	Maximum Voltage

Permanent Magnet Synchronous Generator

L_d	*d*-axis inductance
L_q	*q*-axis inductance
R	Resistance of the stator windings
i_{sd}	Stator d-axis current
i_{sq}	Stator q-axis current
v_{sd}	Stator d-axis voltage
v_{sq}	Stator q-axis voltage
ω_r	Angular velocity of the rotor

ϕ_v	Rotor Flux
p	Number of pole pairs
T_g	Electromagnetic torque

Wind Energy Conversion

i_p	PMSG output current after uncontrolled rectifier
v_p	PMSG output voltage after uncontrolled rectifier
i_0	Output of the boost converter
L_B	Line inductance of the dc-dc boost converter
C	Capacitance
v_{dc}	Voltage output of the boost converter
P_m	Mechanical power produced by wind turbine
ρ	Air density
v_w	Wind speed
C_p	Power coefficient
λ	Tip speed ratio
ω_r	Rotational speed of the rotor blade
r	Radius of the turbine blade

T_r	Torque produced by wind turbine

Grid Fault Monitoring System

V_{dip}	Voltage dip
e_a, e_b, e_c	Grid voltage
I_r^*	Reactive current reference
$I_{\max}$	RMS value of the maximum current limit of the inverter
S	Maximum apparent power of the three-phase inverter
P^*	Real power reference
Q^*	Reactive power reference
θ	Angle

Grid Side Controller

i_a, i_b, i_c	Grid current
ω	Angular Frequency
e_d	d-axis voltage
e_q	q-axis voltage

i_d	d-axis current
i_q	q-axis current
e_d^+	Positive sequence d-axis voltage
e_q^+	Positive sequence q-axis voltage
e_d^-	Negative sequence d-axis voltage
e_q^-	Negative sequence q-axis voltage
i_d^+	Positive sequence d-axis current
i_q^+	Positive sequence q-axis current
i_d^-	Negative sequence d-axis current
i_q^-	Negative sequence q-axis current
P_0	Average value of instantaneous active power
Q_0	Average value of instantaneous reactive power
P_C, P_S	Oscillating components of real power
Q_C, Q_S	Oscillating components of reactive power

List of Abbreviations

AC	Alternating current

ANN	Artificial Neural Network
CSC	Current Source Converter
DC	Direct Current
DER	Distributed Energy Resource
DG	Distributed Generators
DFIG	Doubly Fed Induction Generator
EMF	Electromotive Force
FLC	Fuzzy Logic Controller
GW	Gigawatts
GSC	Grid Side Controller
HIL	Hardware-in-Loop
IGBT	Insulated Gate Bipolar Transistor
LVRT	Low Voltage Ride Through
MPP	Maximum Power Point
MPPT	Maximum Power Point Tracking
MSC	Machine Side Controller
PI	Proportional-Integral
PLL	Phase Locked Loop
PR	Proportional Resonance

PMSG	Permanent Magnet Synchronous Generator
PS	Pure Simulation
PV	Photovoltaic
PVECS	Photovoltaic Energy Conversion System
PWM	Pulse Width Modulation
RCP	Rapid Control Prototyping
RMS	Root Mean Square
RT	Real Time
SCIG	Squirrel Cage Induction Generator
SPWM	Sinusoidal Pulse Width Modulation
VSC	Voltage Source Converter
WECS	Wind Energy Conversion Systems

Chapter 1: Introduction

1.1. Background and Motivation

Climate change challenge, scarcity of energy resources, access to electricity, and an ever-increasing demand for electric power require widespread use of renewable energy technologies. Fossil fuel based power plants produce tons of greenhouse gasses, which are directly responsible for global warming. Statistics show that about 67.4% of total electricity comes from burning fossil fuels that contribute 40% of total greenhouse gas emission [1] [2]. According to World Bank, around 1.1 billion people still do not have access to electricity due to unavailability of the grid in these areas and other constraints [3]. Besides, International Energy Agency predicts that world electricity consumption will increase by about 36% from 2013 to 2030 [4]. In recent United Nation Framework on Climate Change Conference COP21, a collective goal is set to keep the global warming below 2°C compared to pre-industrial times and pursuing efforts to limit the temperature rise to 1.5°C [5]. Thus, promoting renewable energy technologies and development of efficient renewable energy conversion system are two crucial steps to overcome global warming challenges [4], [5]. Renewable technologies like solar photovoltaic (PV), wind energy, geothermal, and tidal energy are considered as clean sources of energy. They provide an excellent opportunity for the mitigation of greenhouse gas emission by

substituting fossil fuel based power plant. Solar and wind energy are the two most popular renewable energy resources due to wide availability, easy installation, and long lifetime.

A Solar Photovoltaic Energy Conversion System (PVECS) system is a safe, reliable, and low-maintenance source of electricity that produces no on-site pollution or emissions. It can generate the power from microwatts to megawatts. Since the scaling of input power source is easy, solar PV system is an excellent choice in remote areas for low and medium level power generation [6]. Basically, the solar cell is a p-n semiconductor junction that directly converts solar irradiation into direct current (DC) using the photovoltaic effect [7]. Several solar cells are connected in series-parallel and then encapsulated in an especial frame to construct the PV panel [8].

A Wind Energy Conversion System (WECS) converts the motion of the wind flow into electricity [9]. A wind turbine allows transforming the motion of the wind flow into a rotational motion. It is directly coupled to an electric generator that generates electric power. The power generated from the WECS is directly proportional to the wind speed. There are three types of generators are used widely in wind energy application: squirrel-cage induction generator (SCIG), doubly fed induction generator (DFIG), and Permanent Magnet Synchronous Generator (PMSG) [9]–[12]. The SCIG based wind turbine is a fixed speed wind turbine that requires a multi-stage gearbox [13]. The DFIG based wind turbine is a variable speed wind turbine system also with a multi-stage gearbox, where the power electronic converter feeding approximately 30% power rating of the generator capacity from the rotor winding, whereas the stator winding is directly connected to the grid [14]. The PMSG based wind turbine is also a variable speed that requires a full-scale power

electronic interface [14]. Apart from above-mentioned generators, DC generators are used to some extent [15], [16]. However, it is unusual for wind turbine applications [11]. Among the mentioned types, the PMSG is more efficient and it does not require a gearbox [18].

The solar irradiance, temperature, and wind speed are continuously changing. As the PV and wind power are the intermittent sources, the intermittency may cause instability in an electrical power generation system [19], [20]. A proper control and power electronic interface play a crucial role for the PV and wind electric power system.

1.2. Literature Review

1.2.1 Photovoltaic Energy Conversion System

Nowadays the PVECS is becoming a very popular renewable source because of its efficiency increasing and price decreasing over time. Moreover, it is easy to install PV panel on roofs/properties. The global growth of the PV has been fitting an exponential curve for more than two decades. By the end of 2016, the cumulative photovoltaic capacity reached at least 227 gigawatts (GW), which is sufficient to supply 1% of global electricity demands [13]. According to the International Energy Agency, about 65.7 GW global PV deployment is forecasted in 2017 [13]. It is projected to more than double or even triple beyond 500 GW between now and 2020 [14]. The PVECS continues its impressive and dynamic development in technology, industry, applications, installed capacity, and price as well as great business opportunity.

A PV System consists of one or several PV modules, connected to either an electricity network or to a series of loads. It comprises of various electric devices aiming to adapt the electricity output of the modules to the standards of the network or the load: inverters, converters, or energy storage systems. The PV power system is classified into two types as described in [21]

- Stand-alone system
- Grid-connected system

The stand-alone PV system requires energy storage system to provide power during low-light periods [22], whereas, a grid-connected PV system doesn't require energy storage system [23]. A Maximum Power Point Tracker (MPPT) continuously adjusts the load impedance to provide the maximum power from the PV array for the both cases. Nowadays, more than 99% of PV systems are grid-connected [24]. They are more cost-effective and require less maintenance and reinvestment than stand-alone systems.

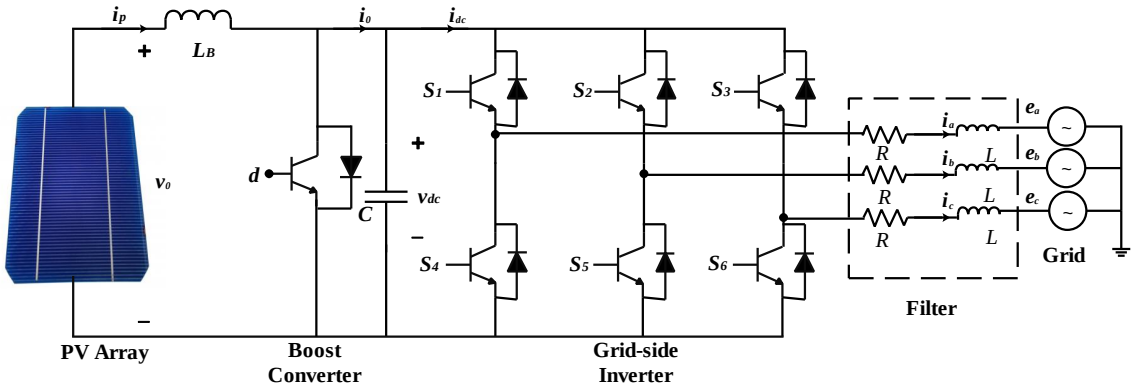

Figure 1 Grid-connected PVECS

The grid-connected PV system includes a PV module, an MPPT boost converter, grid side inverter, filter, and grid as is shown in Figure 1. An inverter is used to convert electricity from DC as produced by the PV array to alternating current (AC) that is then supplied to the electricity network. A line filter is used to remove the high-frequency component of the supplied power to the grid.

1.2.1.1 Basic Control of Grid-Connected Photovoltaic Systems

The control system for the grid-connected PV system can be divided into two major types

- DC-DC boost control
- Grid-side control

The dc-dc boost converter decouples the PV system from the grid control. Additionally, it can boost the PV voltage, provide galvanic isolation, and perform MPPT control [24]. In a PV system, MPPT techniques maximize continually the PV array output power, which generally depends on solar radiation and cell temperature. Figure 2 depicts the I–V characteristic and power versus voltage curve of a single solar cell. It indicates that the solar PV can give maximum power only at a single point. For extracting the maximum power from the cell, the operating voltage and current should be corresponding to the maximum power point (P_{max}) i.e. v_m and i_m respectively under a given temperature and insolation [6], [26].

The PV MPPT techniques can be classified as indirect control, direct control, and soft computing techniques based on their control strategy [27]. The indirect control methods are typically based on mathematical relationship obtained from the empirical data, which

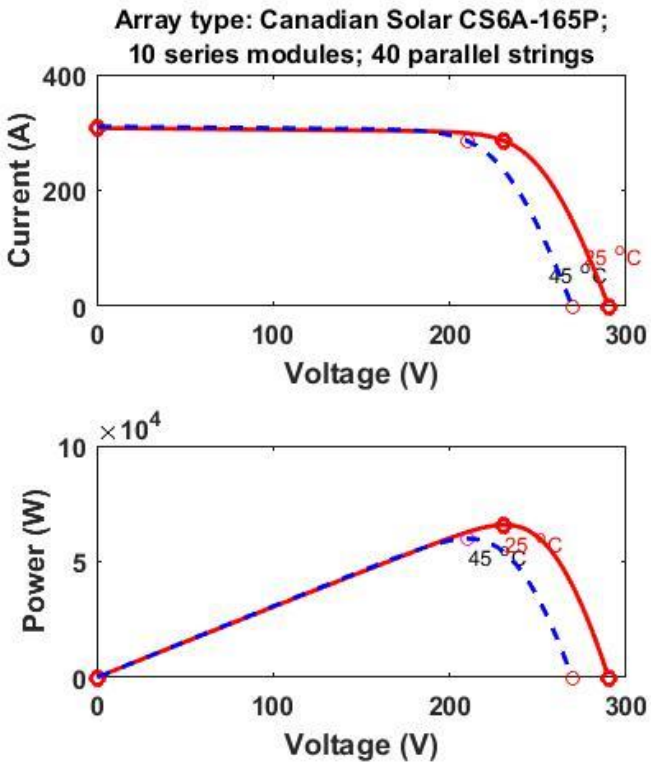

Figure 2 Solar cell I–V and P–V characteristic

may include the parameters and characteristic of the solar PV panel. Maximum power points are predicted offline using various algorithms, empirical data, or mathematical equations. These methods are not suitable for fast changing environmental condition and partial shading condition [27]. Constant voltage, constant current, look up the table, curve fitting, and pilot cell methods are the examples of indirect MPPT techniques.

The direct control methods find the maximum power points at different atmospheric conditions from the real-time data. Generally, they have a sampling based control or modulation based control strategy. Hill climbing, perturb & observe, and incremental conductance methods are some examples of direct control MPPT [28]. They are the most

popular and widely deployed in several commercial grids- tied and stand-alone applications.

Fuzzy logic controller (FLC) and artificial neural network (ANN) are soft computing based MPPT techniques [27], [29]. The ANN is highly complicated because the multilayered network that requires training to correctly respond to different irradiance, temperature, and other PV inputs [30]. If the training is sufficient and correctly done, the accuracy of the MPPT can be very high [31]. On the other hand, a standalone FLC algorithm is considerably simpler but its tracking performance is inferior to a well-trained ANN [27]. Accordingly, there is a trade-off between the performance, cost, and simplicity of the design of MPPT.

The grid-side controller is a crucial part of the grid-connected PV system. The grid-side controller can have the following tasks [32], [33]:

- control of the active power delivered to the grid
- control of the reactive power exchange with the grid
- high efficiency and high quality of the injected power
- grid synchronization, and anti-islanding protection

The control strategy applied to the three-phase PV inverters involves two cascaded loops; outer loop and inner loop [34]. The outer loop is responsible for the voltage control and the inner loop is responsible for the current control [35]. The implementation of the control strategy for the three-phase PV inverter can be done in three reference frames- synchronous rotating (*dq*), stationary (*αβ*), and natural (*abc*) [34]–[37].

The Park transformation to a three-phase variable (grid voltage and current) leads to the possibility of *dq*-control for a three-phase system [34]. Most of the control use an *abc* to *dq* transformation to transform the grid voltage and current waveforms into a reference frame that rotates synchronously with the grid voltage. Consequently, the control variables become DC quantities. Since every deviation of the grid voltage and/or the grid current will be reflected in the corresponding *d*-axis and *q*-axis components, it leads to an easy solution to filter and control by means of Proportional-Integral (PI) based controllers. A phase locked loop (PLL) is used to lock on the grid frequency and provide a stable reference synchronization signal for the inverter control system, which works to minimize the error between the injected current and the reference current obtained from the DC link controller.

Another implementation of the control loops can be done in a stationary reference frame, also known as $\alpha\beta$ control [34]. In this control structure, the control variables (e.g. grid voltage and current) are transformed from *abc* to $\alpha\beta$. The resultant components in the $\alpha\beta$ reference frame are sinusoidal. Since the PI controller is not good at removing the steady-state error when the signal is time varying, employment of other controllers i.e. Proportional Resonance (PR) controller is necessary [38].

In the natural reference control strategy (*abc*-control), an individual controller is applied to each grid current [34]. However, the configurations of the three-phase system structure, e.g. delta or star configuration make a challenge for the design of the three individual current controllers. The DC-link voltage is controlled to generate the active current reference. Then, the current references in *dq*-frame are transformed into three

current references using the inverse Park transformation and the phase angle of the grid voltages. Each of the current references is compared with the corresponding measured grid current, and the error goes into the current controller, forming the reference pulse width modulation (PWM) signal for the three-phase PV inverter. The existing controllers, such as PI controller, PR controller, hysteresis controller, deadbeat controller and the repetitive controller can be adopted as the three current controllers in the natural reference frame control structure [32], [36]. Selection of those above-mentioned control strategy is dependent on the control complexity and dynamic performance of the system.

1.2.2 Wind Energy Conversion System

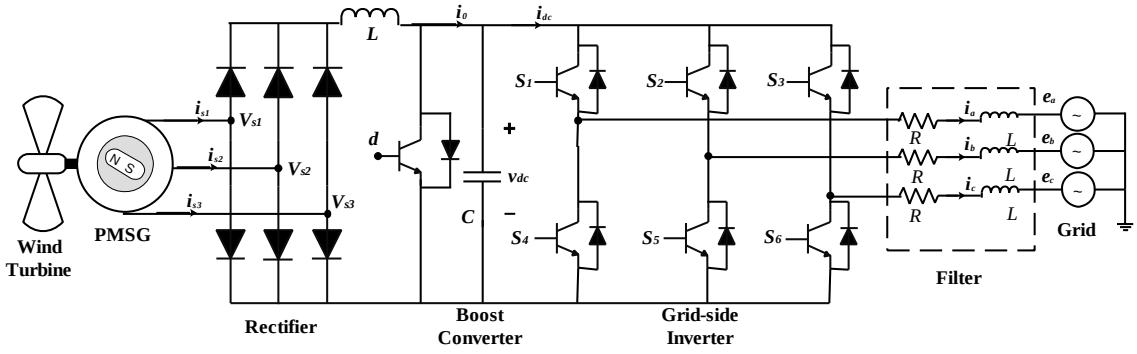

Figure 3 Grid-connected WECS

Wind power is a mature technology with proven reliability and cost effectiveness that makes it a very attractive option for utilities, independent power producers, and companies. The WECS leads all renewable technologies among the all renewable technologies; more than 50 GW wind power capacity was installed in 2016 and about 330 GW total capacity will be added by 2021 [39]. The WECS has been proven a success story in the industry.

The typical grid-connected wind system includes a wind turbine, generator, machine side converter, grid side inverter, filter, and grid that is shown in Figure 3. The wind energy system is connected to the grid through converters. The rated output power of the wind turbine can be achieved at rated wind speed. The wind generator generates power by the rotation of the wind turbine [40]. Operating region of WECS is classified into four regions as shown in Figure 4. The WECS produces power in region 2 and in region 3 [41].

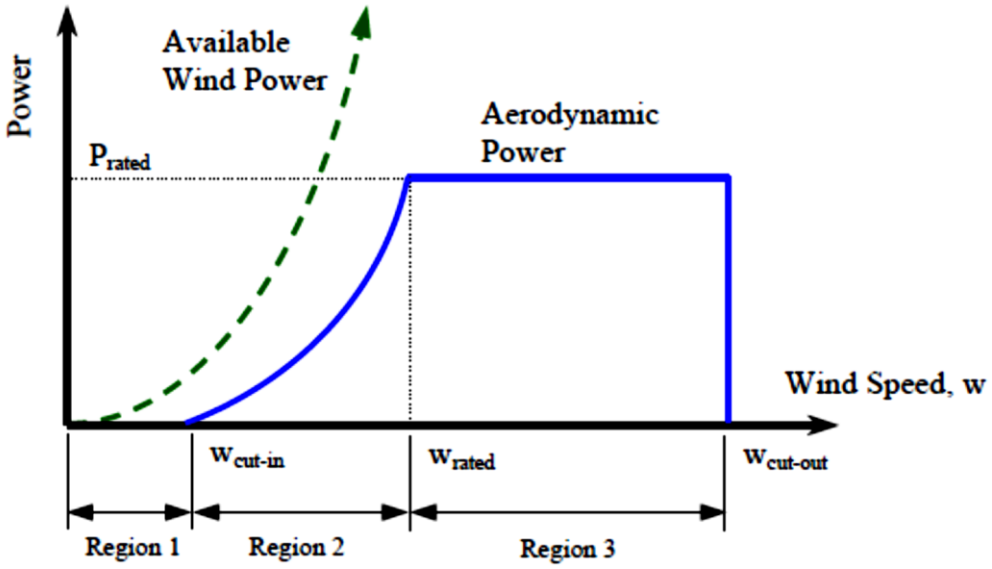

Figure 4 Operating regions of WECS

1.2.2.1 Basic Control of Grid-Connected Wind Power Systems

The PMSG based WECSs are preferred full-scale converters since the power converters fully decouple the wind turbine from the grid disturbances [42]. The full-scale power converter offers high reliability and good power quality also it may avoid the bulky grid-side transformer [43].

The control structure of the wind generator can be divided into two categories [44]

- Machine-side control
- Grid-side control

Several types of power electronic interfaces are presented in the literature for direct-driven variable-speed PMSG based WECSs [45]–[52]. A typical configuration of PMSG based WECS with ac–dc–ac converter must consist a machine (generator)- side converter (MSC) and a grid-side converter (GSC) interconnected through a common dc-link element, which can either be an inductor in case of current source converter (CSC) or a capacitor in case of voltage-source converter (VSC) based configurations [53].

Among different high power and medium voltage power converter topologies the CSC based ac–dc–ac converter configuration appears to be a promising solution owing to simple topology, low device number, high power capability, reliable short circuit current protection, and inherent four quadrant operation ability [49]–[51]. On the other hand, the diode rectifier based unidirectional converters with a boost converter and the back-to-back IGBT based two-level VSCs are the most popular topologies among others. The back-to-back VSCs used in the PMSG-based WECS minimizes the electromagnetic torque ripples in the generator and improves the power controllability, enhances the power quality by reducing the current harmonics. However, diode rectifier based unidirectional converters with a boost converter is a simple and low-cost solution and widely used in the industry [53]. It also aids to the low voltage ride through (LVRT) capability of the grid-connected WECS.

1.2.3 Low Voltage Ride Through Capability

The continuously increasing capacity of the distributed energy resources (DERs) now contributes a significant amount of power to the grid. The LVRT capability has become a crucial issue as more DERs are installed in the grid [54]. Conventionally, the distributed generators (DGs) are disconnected from the grid during grid faults and reconnected to the grid after clearing the faults [55]–[57]. However, disconnection causes huge power loss and voltage instability [58]. Thus, many countries have revised the grid code; DGs might be connected to the grid and support the grid during grid fault that is known as LVRT [35], [59], [60]. Grid regulations demand to supply reactive power by injecting reactive current during fault conditions to support grid stability [61].

The grid faults can be classified into two categories; symmetrical/balanced fault and asymmetrical/unbalanced fault [32]. The symmetrical fault is the same voltage drop on all phases whereas the asymmetrical fault is an unequal voltage drop with phase shifting between faulty phases. The unsymmetrical grid voltage dips give rise to unbalanced grid voltage as the negative-sequence components appear in the grid voltage. The presence of negative-sequence components causes a negative-sequence current and ripple in the power injected to the grid. This causes grid current peaks and dc bus voltage fluctuations, which may cause uncontrolled oscillations in the active and reactive power delivered to the network [34]. However, the injection of a proper set of unbalanced currents under voltage dips removes attenuating power oscillations [62].

Several control techniques with different fault monitoring techniques and grid synchronization have been studied in the literature in order to assure a proper exchange of active and reactive power and to keep the grid voltage and frequency under control. The LVRT operation of the grid-connected wind turbines and PV system with the vector current controller was presented in [63], [64]. However, these works did not consider unsymmetrical faults and power oscillations to control the current under unbalanced voltage conditions. The controlling of the double-frequency power oscillations in the dc-link voltage converter under unbalanced grid voltages is a crucial part to mitigate the dc-link ripple and power oscillation. However, it worsens the performance of the distributed generators and the converters without proper control.

The instantaneous active-reactive power control and the instantaneously controlled positive sequence method using the positive and negative sequence current control are described in [34], [65]. However, these two techniques can create harmonics under unbalanced grid voltages. In order to eliminate the low-order harmonics in grid currents, the root mean square (RMS) of grid voltages are used in the average active reactive power control [66]. The average active-reactive power control method reduces the grid current amplitude, but it could result in oscillations in the grid power. A positive and negative sequence power control that can provide power and sinusoidal grid currents without the oscillation using a proper set of positive and negative sequence grid current references [67]. However, supplying the real and reactive power without limiting current may damage the grid inverter and activate the overcurrent protection [68].

The active and reactive power limiters were introduced in [69] to eliminate over current in the grid inverters. In this structure, a crowbar was used to dissipate the surplus generated power. However, high-performance control schemes to operate the converters efficiently under grid fault conditions can remove the additional use of a crowbar. In addition, a reactive current injection method without exceeding the current limit of the inverter was proposed in [70]. However, the power balance between the power generated by the distributed generators and the power delivered into the grid under grid faults are not considered in the above references. The active and reactive power control of three-phase grid-connected PV system during grid faults using PI and fuzzy neural network control is demonstrated in [71]. They showed power balance and supplying reactive power for the PV without exceeding the maximum current rating of the inverter. However, they did not consider positive and negative sequence control that is essential for the unsymmetrical fault.

1.3. Objective and Contribution of the Research

The main purpose of this research is to design a control system for the grid connected PV and wind power system with LVRT capability and verify the design with laboratory scale PV and PMSG system through rapid control prototyping. The objective and scope of the work are as follows,

1. Development of the control interface of the grid connected PV and wind power system

The mathematical modeling of the MPPT of the PV module and machine side controller of the PMSG as well as grid side controller for the PV and PMSG system is designed in the Simulink software. Then the designed control system is applied in the experimental system.

2. Implementation of grid fault monitoring system with grid support

The proposed research work includes a grid fault monitoring system that detects the grid fault and generated suitable real and reactive power reference as per grid code with protecting grid side inverter.

3. Development of the control interface of the grid connected PV and wind Power system under grid fault

The grid control system facilitates grid support during a grid fault. The grid connected PV and PMSG system supply real and reactive power to the grid during a grid fault. Also, the dc-link control system keeps the dc-link voltage constant.

Thesis Contribution: This research work reports on the design and practical implementation of the grid connected PV and wind power system. The main contribution of the work is the design and implementation of a control system with the grid fault monitoring system. The proposed system has two modes- normal mode with MPPT and faulty mode with grid support. A dual current controller is designed for controlling positive and negative sequence components under grid fault in order to deal with the asymmetrical faults. It permits the injection of the reactive current to the grid according to the reactive current requirement of grid codes in symmetrical and asymmetrical grid

faults. The controller for the faulty condition is designed in such a way that the inverter current never exceeds the current rating of the inverter to protect it during a grid fault. In addition, the real and reactive power references in faulty mode are based on the grid voltage sag conditions and maximum current rating of the inverter. Moreover, the proposed structure has good performances in different types of asymmetrical faults. Besides, the active power oscillation and dc-link voltage ripple can be suppressed by using proposed control system.

1.4. Outline

This thesis report consists of six chapters. Chapter wise descriptions are given below:

Chapter One

In the first chapter, the background and motivation, literature review, objectives, and contribution of the thesis are discussed in detail.

Chapter Two

The second chapter is studied about the grid code requirements of the grid connected PV and wind power system, details of the grid fault, and the fault monitoring system.

Chapter Three

The third chapter focuses on system modeling that includes mathematical modeling of the Solar PV module, Wind turbine, Permanent magnet synchronous generator, Boost converter, and three-phase inverter

Chapter Four

Chapter four describes the dual mode control system for grid-integrated renewables. It includes MPPT for PV, machine side controller for PMSG, and grid side controller under normal grid condition. It also consists of dc-link voltage controller for the PV and PMSG as well as grid side controller under grid fault condition.

Chapter Five

The experimentation and result of the research are described in this chapter. Starting with a rapid control prototyping system, this chapter discusses the hardware details, real-time simulation environment, and RT-Lab modeling. Finally, the experimental result of the thesis is presented for the both PV and wind system.

Chapter Six

This chapter concludes the thesis with a brief summary of the work and the suggestions of the future work.

Chapter 2: Grid Code Requirements and Grid Fault Monitoring System

2.1. Introduction

The grid requirements for integration of renewable energy systems (PV and wind turbine system) to the electric power grid are becoming more stringent due to the increasing demands of the clean and reliable electricity generation. The grid integrated DGs must comply with a series of standard requirements in order to ensure the safety and continuous transfer of the electrical energy to the grid. Typically, local regulations are imposed by the grid operators and apply in the most countries. However, large efforts are made worldwide to impose some standard grid requirements that can be adopted by various countries.

In this chapter, specific requirements for the PV and wind power systems are addressed, then the details of the grid fault and fault monitoring system are discussed. Finally, the conclusion is drawn in the last section of the chapter.

2.2. Grid Requirements for Grid-Connected Photovoltaics

The PV systems are considered a minor part of the overall electricity generation. Therefore, the distribution/transmission system operators impose basic grid codes in order to assure the quality of the generated power. According to IEEE 1547 (Standard for Interconnecting Distributed Resources with Electric Power Systems), the following parameters are required for designing the control of PV inverters [72]

- Voltage harmonic levels (h): $h < 11 = 4\%, 11 \leq h < 17 = 2\%, 17 \leq h < 23 = 1.5\%, 23 \leq h < 35 = 0.5\%, 11 \leq h < 35 = 0.3\%$
- Maximum voltage Total harmonic distortion (THD): maximum 5%
- Voltage amplitude variations: maximum ±5%.
- Frequency variations: 59.3 Hz to 60.5 Hz
- Direct current injection: maximum 0.5%

In normal operation, the PV systems should maximize the output power with MPPT technique. The PV systems are currently required to disconnect from the distributed grid for safety reasons during abnormal grid conditions, which is known as the islanding protection.

2.3. Grid Requirement for Grid-Connected Wind Power

The most common requirements for the grid-connected wind power system include LVRT capability, voltage and frequency control, and active-reactive power control. The frequency and voltage control requirements demand the WECS should operate within a range around the rated voltage and frequency. The grid regulation for the active and reactive power control demand the wind power system should regulate the active and reactive power in response to the wind speed variation and grid voltage variation. For the small-scale wind power system, the grid code is same as PV system that described in the previous section.

2.3.1. LVRT requirements of the Different Grid Code

There is specific grid code of the LVRT capability for large PV and wind power generation system. Different countries have different LVRT requirements for the large-scale WECS. For an example, the German code from E. ON [54], LVRT applies to a network with voltage levels 380 kV, 220 kV, and 110 kV. Whereas according to Canadian Hydro-Quebec grid code [73], LVRT applies to networks with voltages above 44 kV. There is no strict LVRT requirement for the low-voltage WECS. As low-voltage DGs are growing rapidly, the present active grid codes are expected to be modified in order to accept more clean energy into the grid. It is better to provide LVRT capability requirements for low-voltage DGs in order to ensure reliable and efficient power system.

The LVRT requirements demand the WECS must withstand voltage dips down to a certain percentage of the nominal voltage for a specified duration during a grid fault. It also includes fast active and reactive output power restoration to the pre-fault values after the system voltage returns to normal operation. Certain codes impose increased reactive current generation by the wind generators during the disturbance to support the system voltage. Normally, the reactive power support must be satisfied with the highest priority during a fault operation. The active power generation can be reduced in order to fulfill this requirement. Figure 5 shows the LVRT requirements of different national grid codes [74].

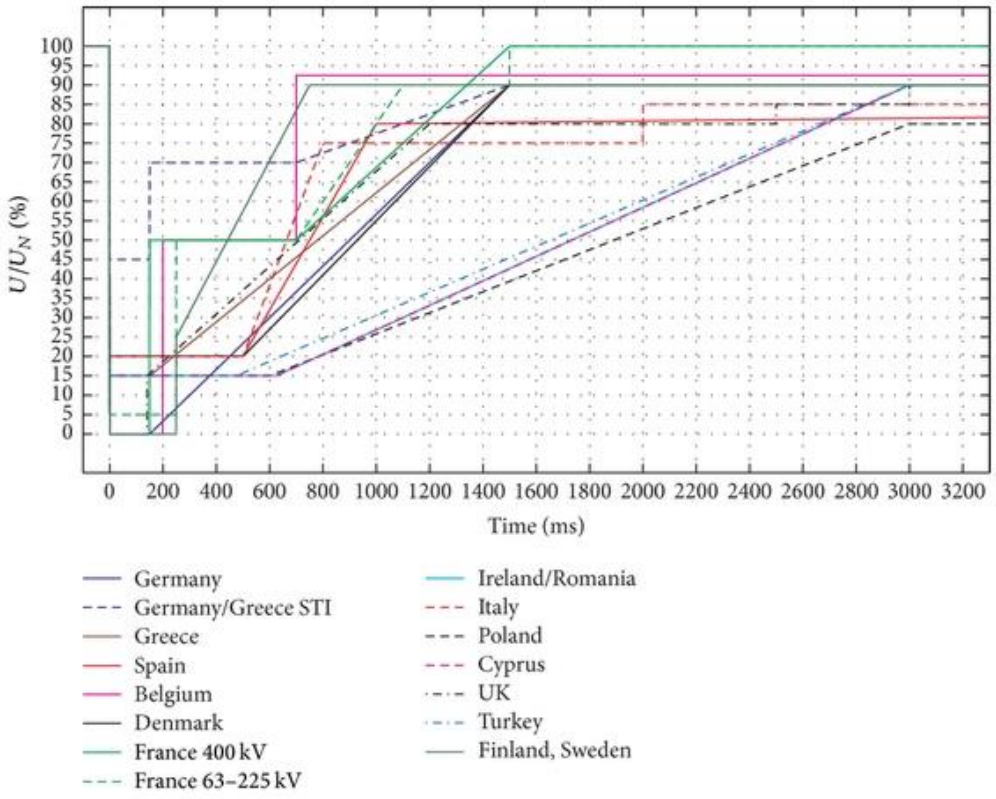

Figure 5 National grid codes and their pattern

Table 1 Characteristics of fault ride-through in various grid codes

Country	**Fault Duration (*ms*)**	**Fault Duration (*cycles*)**	**Min Voltage Level *(% of V_{nom})***	**Voltage Restoration (*s*)**
Canada (AESO)	625	37.5	15	3
Canada (Hydro Quebec)	150	9	0	1
Germany (E. ON)	150	7.5	0	1.5
UK	140	7	0	1.2
USA	625	37.5	15	3
Ireland	525	31.25	15	3
Nordel	250	12.5	0	0.75
Denmark (<100 kV)	140	7	25	0.75
Denmark (>100 kV)	100	5	0	10
Belgium (Large voltage dips)	200	10	0	0.7
Belgium (Small voltage dips)	1500	75	70	1.5
Sweden (<100 MW)	250	12.5	25	0.25
Sweden (>100 MW)	250	12.5	0	0.8
New Zealand	200	10	0	1
Spain	500	25	20	1
Italy	500	25	20	0.8

Table 1 summarizes the most grid codes concerning LVRT capability for the high-voltage level system that is shown in Figure 5. The requirements depend on the specific characteristics of each power system and they deviate significantly from each other. The

requirements of the German, Hydro Quebec, UK, Nordic, Danish, Belgian, Swedish, and New Zealand grid codes demand the WECS must remain connected during voltage dips down to 0%. The corresponding voltage dip at a lower voltage is above 15% considering impedance values for the step-up transformers and interconnecting lines [75]. However, specifications may vary according to the voltage level or the wind farm power. For an example, the wind farm connected to the Danish grid at voltages below 100 kV are required to withstand less severe voltage dips than those are connected at higher voltages. Similar differences can be observed in the regulation governing the connection of wind farms below and above 100 MW in the Swedish transmission systems. The codes of Denmark and Hydro-Quebec define specific types and sequences of faults that the wind farm must withstand including remote faults cleared by slow protective devices.

There is a significant difference in the active power restoration rates specified by the German and British/Irish grid codes. The British code requires immediate restoration at 90% in 0.5 s after voltage recovery because of the instability of the weakly interconnected transmission system [76]. Whereas German code requires restoration with a rate at least equal to 20% of the nominal output power reaching 100% in 5 s after voltage recovery [54].

2.3.2. Requirements for Reactive Current Supply During Voltage Dips

Some grid codes recommend the WECS should support the grid by generating reactive power to restore fast grid voltage. For an example, German grid code from E. ON [54]

requires the WECS support grid voltage with additional reactive current (reactive power) during a voltage dip which is shown in Figure 6. The grid support must take place within one cycle after fault recognition amounting to at least 2% of the rated current for each percent of the voltage dip. A reactive power output of at least 100% of the rated current must be possible if necessary. The above applies outside a ±10% dead band around nominal voltage. In the case of offshore wind farms, the dead band is reduced to ±5%. According to the Spanish grid code, the wind power plants are required to stop drawing reactive power within five cycles of a drop voltage and to be able to inject reactive power within 7.5 cycles of grid recovery. Finally, Great Britain and Ireland specify in their grid codes that wind farms must produce their maximum reactive current during a voltage dip caused by a network fault.

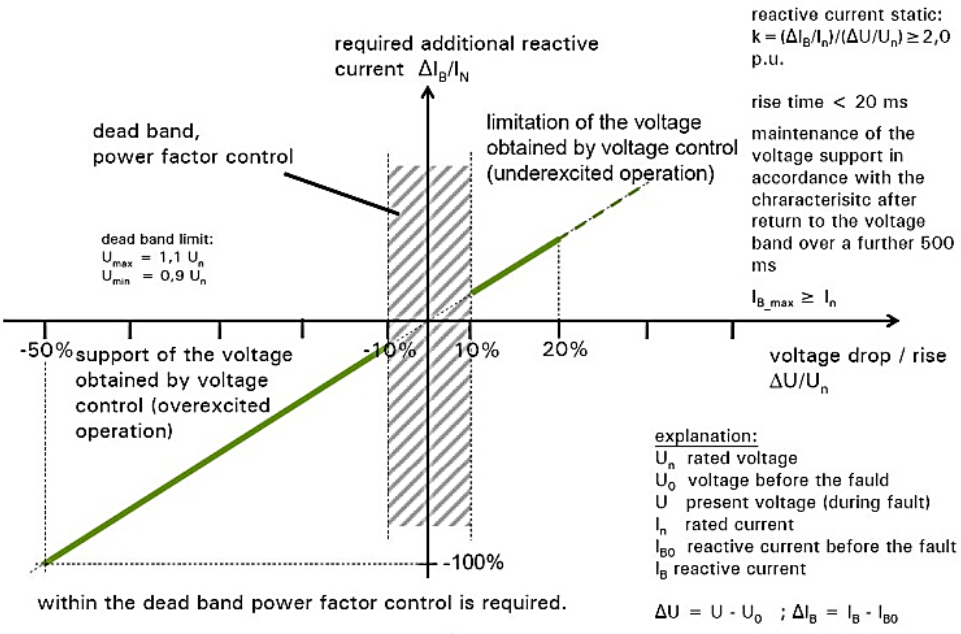

Figure 6 Reactive output current during voltage disturbances according to the E. ON grid code

2.4. Types of Grid Faults

The grid sags can be categorized into four fault types as follows [77]

- Single phase to ground fault
- Two-phase to ground fault
- Three-phase to ground fault
- Phase to phase fault

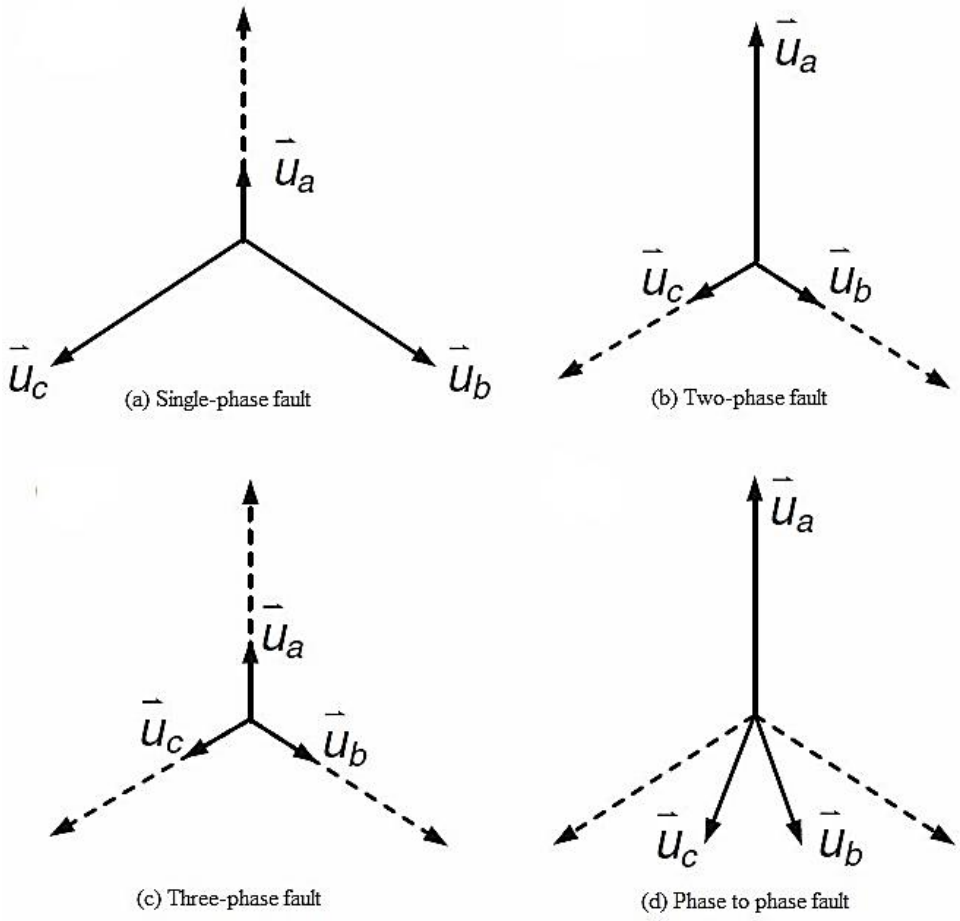

Figure 7 Typical voltage sag types in three-phase systems

According to Figure 7, the grid faults can be classified into two major categories; symmetrical/balanced fault and asymmetrical/unbalanced fault [78]. Symmetrical fault represents the same amplitude drop on all three grid voltages but no phase shifting. It occurs very seldom in the three-phase systems. The asymmetrical fault occurs when the phase voltages have unequal amplitude with phase shifting between the faulty voltages. This fault is induced by one or two phases shorted to ground or to each other. When an asymmetrical fault occurs, the negative sequence appears in the grid voltages and thus increases the control complexity. Since the implementation of these strategies gives rise to the injection of unbalanced currents to the grid, specific current control structures should deploy to regulate the positive and negative sequence components.

2.5. Grid Fault Monitoring System

The grid faults are characterized by a short-time reduction in the magnitudes of the grid voltage phases, called voltage dip (or sag), and can be caused by faults in the grid lines [35]. The voltage dip is expressed for the phase voltages as follows [71]

$$V_{\text{dip}} = \left(1 - \frac{\min\left(|e_a|_{\text{rms}}, |e_b|_{\text{rms}}, |e_c|_{\text{rms}}\right)}{E_{\text{base}}}\right) \text{p.u.} \tag{2.1}$$

where V_{dip} is voltage dip, E_{base} is the base value of the voltage (grid rated voltage during normal conditions), $|e_a|_{\text{rms}}$, $|e_b|_{\text{rms}}$ and $|e_c|_{\text{rms}}$ are the RMS values of the three-phase voltages e_a, e_b and e_c, respectively.

A reactive current is injected to the grid to avoid excess current in the inverter, and it is related to the level of voltage dip [60]

$$I_r^* = \begin{cases} 0, & V_{\text{dip}} \le 0.1 \\ 2V_{\text{dip}}, & 0.1 < V_{\text{dip}} \le 0.5 \\ 1, & V_{\text{dip}} > 0.5 \end{cases} \tag{2.2}$$

where, I_r^* is the reactive current and V_{dip} is the voltage dip.

When I_r^* greater than 0.1 p.u., then a voltage dip occurs on the grid side, and the reactive power injection is initiated. In order to meet the LVRT requirement and avoid exceeding the maximum current limit of the three-phase inverter, the maximum apparent power of the three-phase inverter |S| is obtained by

$$|S| = \left(|e_a|_{\text{rms}} + |e_b|_{\text{rms}} + |e_c|_{\text{rms}}\right) I_{\max} \tag{2.3}$$

Where I_{max} is the RMS value of the maximum current limit.

The LVRT capability consists on active power curtailment, and reactive power injection to support the grid [36], [64]. For this purpose, the active and reactive powers will be regulated as follows

$$\begin{cases} P^* = |S|\sqrt{1 - I_r^{*2}} \\ Q^* = |S| I_r^* \end{cases} \tag{2.4}$$

Therefore, the instantaneous output reactive power and active power of the three-phase inverter Q and P are controlled to follow Q^* and P^* by the proportional–integral (PI) controller.

2.6. Conclusion

In this chapter, different grid code requirements of different countries for grid-connected PVECS and WECS are described briefly. Also, a detailed overview of the grid fault is presented with a view to designing a proper controller for the grid support. Finally, a grid fault monitoring system is designed as per grid code. It is noted that there are no specific LVRT requirements for the low-voltage distributed system. However, low-voltage distributed generators are growing rapidly. Thus, it is better to provide LVRT capability requirements in order to ensure a reliable and efficient power system.

Chapter 3: Dynamic Modeling of the System

3.1. Introduction

Solar photovoltaics converts the solar irradiance into electricity whereas wind generator generates electricity by the rotation of the propeller-like blades (wind turbine) using wind energy. Both solar and wind energy are plentiful, renewable, widely distributed, and produces no greenhouse gas emissions during operation. The net effects on the environment are far less problematic than non-renewable power sources. However, intermittent nature of the solar irradiance and wind energy is a great challenge as solar and wind only produce energy when the sun is shining or the wind is blowing. Moreover, both PV and wind generator are nonlinear sources, they require MPPT technique to extract maximum power from them.

On the other hand, the power converter is a vital part of future power system based on smart grid technologies. It enables efficient and flexible interconnection of different sources (renewable energy generation, energy storage, etc.) to the electric power system. Moreover, it plays a crucial role in the transient behavior of the grid. Thus, modeling the PV module, wind generator, converter, and inverter are an essential part of designing

renewable energy conversion system. This chapter presents a modeling of the PV module, PMSG, converter, and inverter.

3.2. Modeling of the Solar PV module

A solar cell consists of layers of semiconductor materials that exploit the photoelectric effect of converting photon energy of the solar radiation into electricity [79]. It can be considered as a nonlinear current source [80]. The model of a PV cell, using the equivalent circuit of a solar cell in Figure 8, is given by the following equation [81]

$$i_{pv} = n_p i_{ph} - n_p i_{sat}\left(\exp\left(\left(\frac{q}{AKT}\right)\left(\frac{v_{pv}}{n_s} + i_{pv}R_s\right)\right) - 1\right) - \frac{v_{pv} + R_s i_{pv}}{R_{sh}} \tag{3.1}$$

where i_{pv} is the module terminal current, i_{ph} is the photocurrent, i_{sat} is the diode saturation current, v_{pv} is the module terminal voltage, q is the electron charge, A is the diode ideality factor, K is the Boltzmann constant, T is the surface temperature, n_p number of cells in parallel, n_s is the number of cells in series, R_s and R_{sh} are the series and shunt resistances, respectively.

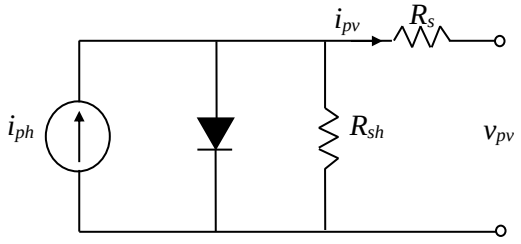

Figure 8 Equivalent circuit of a solar cell

A series-parallel combination of PV module is developed to construct the model of the photovoltaic array. The voltage and the currents across the PV array system are given by

$$\begin{cases} v_0 = N_s V \\ i_p = N_p I \end{cases} \tag{3.2}$$

where N_s is the number of modules in series (string), N_p is the number of strings in parallel, V is the module voltage, and I is the module current.

3.3. Aerodynamic Model of Wind Turbine

The mechanical power extracted from the wind can be expressed as follows

$$P_m = \frac{1}{2} \rho C_p(\lambda, \theta) \pi r^2 v_w^3 \tag{3.3}$$

where P_m is the extracted power from the wind, ρ is the air density (kg/m^3), r is the radius of turbine blades (m), v_w is the wind speed (m/s), and C_p is the power coefficient as the function of the pitch angle of the rotor blades θ (rad) and the tip speed ratio λ.

The tip-speed ratio is defined as

$$\lambda = \frac{r \omega_r}{v_w} \tag{3.4}$$

where ω_r is the turbine rotor speed (rpm). From the expression (3.4), any variation in the wind speed while keeping the rotor speed constant will change the tip-speed ratio. Subsequently, it leads the change in the power coefficient C_p, as well as the generated power from the wind turbine [23], [53]. If the rotor speed is adapted relative to the wind speed variation, the tip-speed ratio can be preserved at an optimum point λ_{opt}, which could yield to maximum power extraction by operating the turbine at the speed reference

$$\omega_{\text{ref}} = \frac{\lambda_{opt}}{r} v_w \tag{3.5}$$

The torque produced by the wind turbine can be expressed using (3.3) and (3.4) as follows

$$T_r = \frac{P_m}{\omega_r} = \frac{1}{2} \rho \frac{C_p(\lambda)}{\lambda} \pi r^3 v_w^2 \tag{3.6}$$

In this study, a 3-blade wind turbine with the power curve is considered as the wind energy source and emulated by a four-quadrant dynamometer through the turbine emulator control function.

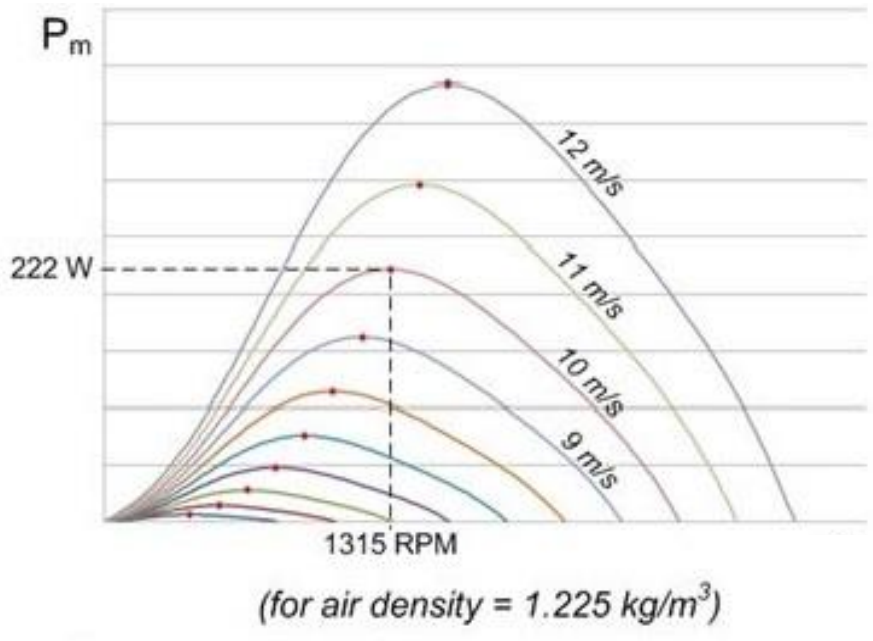

Figure 9 Emulated wind turbine and its power curve

In practice, instead of using the equation (3.5), the speed reference ω_{ref} is generated from a look-up table built from the power curve of the wind turbine, shown in Figure 9, to operate at MPPT.

3.4. Permanent Magnet Synchronous Generator

The rotor excitation of the permanent magnet synchronous generator is constant, so the electrical model of PMSG in the synchronous (*d,q*) reference frame is given by [82]

$$\begin{cases} \dfrac{di_{sd}}{dt} = -\dfrac{R_s}{L_s} i_{sd} + p\omega_r i_{sq} + \dfrac{1}{L_s} v_{sd} \\ \dfrac{di_{sq}}{dt} = -\dfrac{R_s}{L_s} i_{sq} + p\omega_r i_{sd} - \dfrac{1}{L_s} p\omega_r \phi_v + \dfrac{1}{L_s} v_{sq} \end{cases} \tag{3.9}$$

where v_{sd} and v_{sq} are the *d-q* components of the stator voltage; i_{sd} and i_{sq} are the *d-q* components of the stator current; ϕ_v is the permanent magnet magnetic flux linkage, ω_r is the rotor angular speed, R_s is the stator resistance; L_s is the stator winding inductance and *p* is the number of pair poles.

The *d-q* components of the stator current are obtained for the three-phase stator currents (i_{s1}, i_{s2}, i_{s3}), using Park transformation, such as

$$\begin{bmatrix} i_{sd} \\ i_{sq} \end{bmatrix} = \frac{2}{3} \begin{bmatrix} \sin(\theta_e) & \sin(\theta_e - \frac{2}{3}\pi) & \sin(\theta_e + \frac{2}{3}\pi) \\ \cos(\theta_e) & \cos(\theta_e - \frac{2}{3}\pi) & \cos(\theta_e + \frac{2}{3}\pi) \end{bmatrix} \begin{bmatrix} i_{s1} \\ i_{s2} \\ i_{s3} \end{bmatrix} \tag{3.10}$$

where, θ_e is the electrical angle of the vector orientation and carried out using the rotational angular speed ω_r ($\theta_e = \int p\omega_r \, dt$).

The generator torque is expressed as

$$T_e = \frac{3}{2} p\phi_v i_{sq} \tag{3.11}$$

3.5. Boost Converter

The boost DC converter is used to step up the input voltage by storing energy in an inductor for a certain time and then uses this energy to boost the input voltage to a higher value. The circuit diagram for a boost converter is shown in Figure 10.

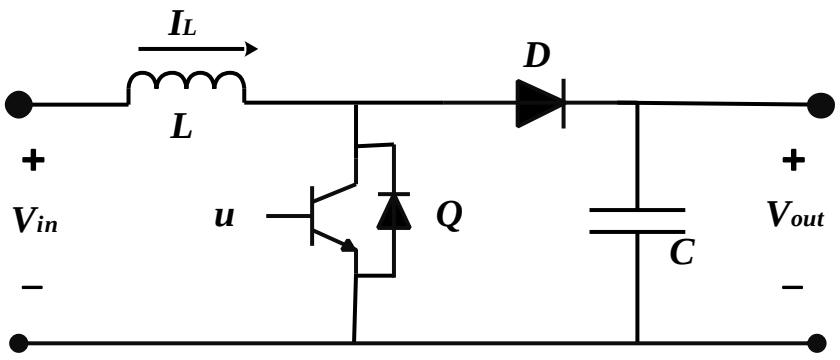

Figure 10 Basic Configuration of Boost Converter

When switch Q is closed, the input source charges up the inductor while diode D is reverse biased to provide isolation between the input and the output of the converter. When the switch is opened, the energy stored in the inductor and the power supply is transferred to the load. The relationship between the input and output voltages is given by

$$V_{in} t_{on} + (V_{in} - V_{out}) t_{off} = 0$$
$$\frac{V_{out}}{V_{in}} = \frac{t_{on} + t_{off}}{t_{off}} = \frac{1}{1-d} \quad (2)$$

where d is the duty cycle, t_{on} and t_{off} are the ON and OFF time respectively.

So, by varying the duty cycle of the buck converter, its output voltage can be varied. MPPT controller generates the duty cycle to operate the boost converter.

3.6. Three-phase Inverter

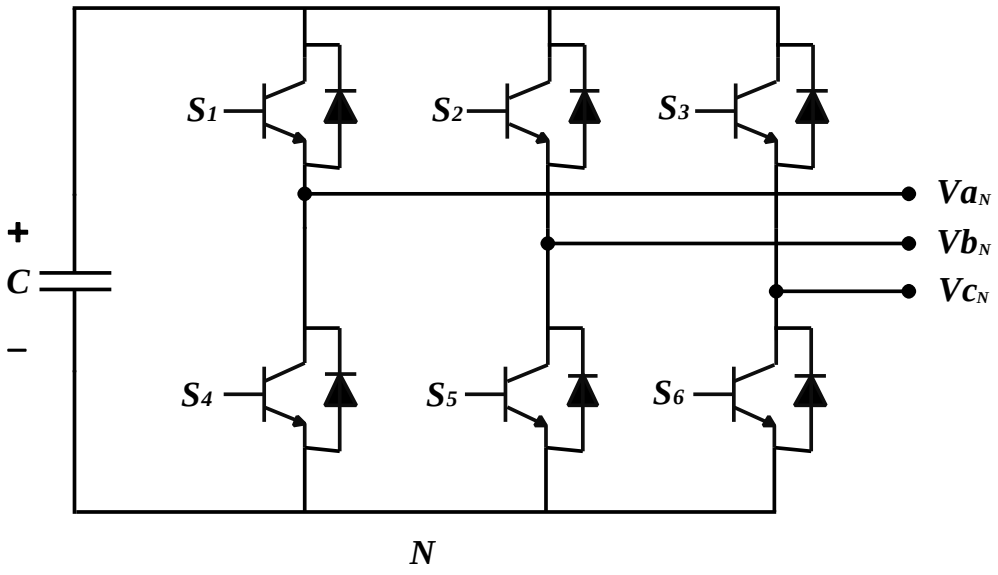

Figure 11 Three phase voltage source inverter

Voltage source inverter (VSI) is mainly used to convert a constant DC voltage into 3-phase AC voltages with the variable magnitude and frequency [83]. Figure 11 shows a schematic diagram of a 3 phase VSI. The inverter is composed of six switches S1 through S6 with each phase output connected to the middle of each “inverter leg”. Two switches in each phase are used to construct one leg. The AC output voltage from the inverter is obtained by controlling the semiconductor switches ON and OFF to generate the desired output. Pulse width modulation (PWM) techniques are widely used to perform this task. In the simplest form, three reference signals are compared to a high-frequency carrier waveform. The result of that comparison in each leg is used to turn the switches ON or OFF. This technique is referred to as sinusoidal pulse width modulation (SPWM). It should be noted that the switches in each leg should be operated interchangeably, in order

not to cause a short circuit of the DC supply. Insulated Gate Bipolar Transistors (IGBTs) and power MOSFET devices can be used to implement the switches [84]. Each device varies in its power ratings and switching speed. IGBTs are well suited for applications that require medium power and switching frequency [85].

3.7. Conclusion

This chapter provided details modeling of the proposed system. The fundamentals of modeling solar PV cell is described at first. Then, the mathematical model of the wind turbine and PMSG wind generator are discussed. Finally, the circuit description of the boost converter and voltage source inverter are presented in this chapter.

Chapter 4: Control System for Grid Integrated Renewables

4.1. Introduction

The intelligent control techniques and power electronics converters in the renewable generation systems (PV and wind power systems) have the responsibility to enable the power conversion effectively and efficiently. The intelligent control techniques are responsible for:

- Maximum power point tracking
- Reliable power supply
- High efficiency, low cost, and effective protection,
- Control of active and reactive power injected into the grid, and
- Dynamic grid support (LVRT) and fault monitoring system.

A detail description of the dual mode control operation of the proposed system is presented in this chapter. The dual-mode control system is illustrated in Figure 12. Under normal grid conditions (mode I), the dc-dc converter will be operated to run under the MPPT, and the grid-connected inverter will be operated through a cascade control loop to control dc-link voltage and *q*-component of the grid current. In grid faults (mode II), the grid inverter is operated via the active and the reactive power control to meet LVRT

requirements. The dc-dc converter is operated using a voltage controller to maintain a constant dc-link voltage.

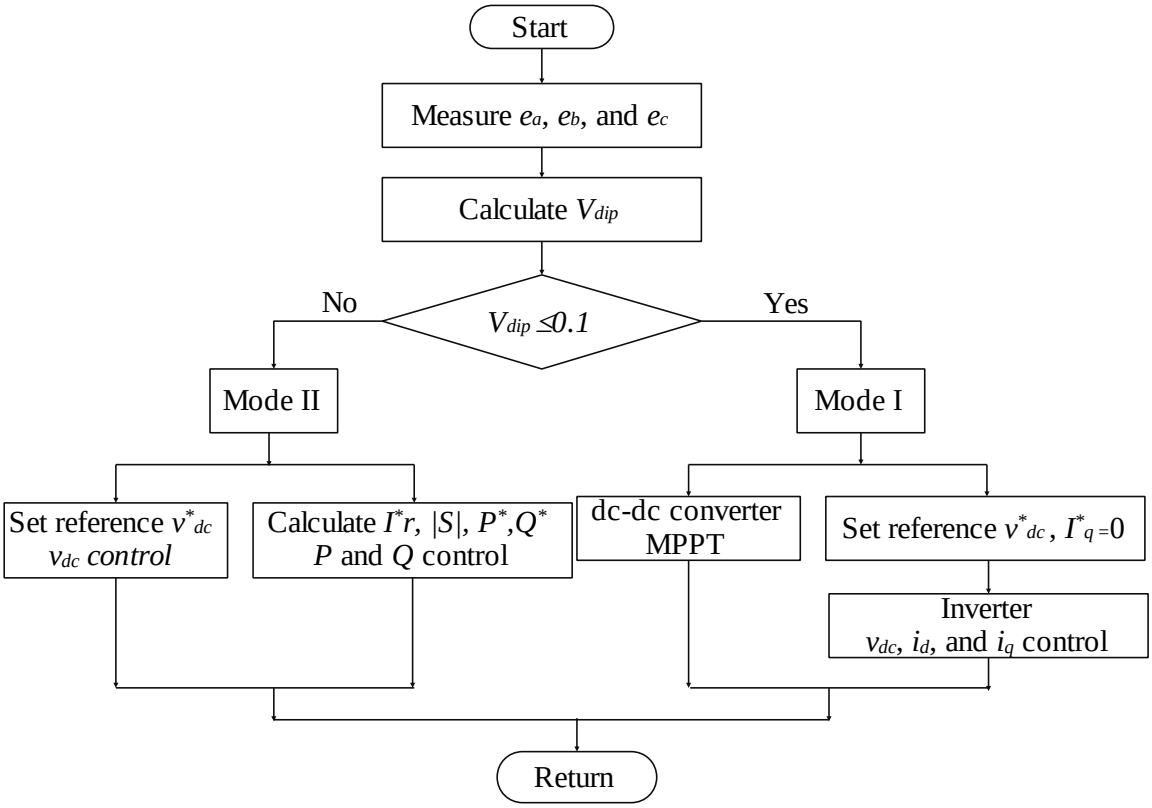

Figure 12 Grid fault monitoring and dual-mode control system

In this chapter, the MPPT technique for the PV and machine side converter of the PMSG are discussed at first. The MPPT for PV and speed controller for PMSG are responsible for extracting maximum power as well as boosted the dc voltage under normal operating condition. The machine side controller includes speed controller and current controller. Then a detailed design of the grid side converter for the PV and PMGS is presented. The control of the three-phase grid-side inverter involves two cascaded loops; voltage control and current control. The voltage controller regulates the DC-link voltage in order to

maintain the power balance between the grid and grid integrated renewable. The current controller takes care of the power quality of the generated power by controlling the injected grid current.

Finally, the control techniques under grid fault condition are described. The power reference is generated by the grid fault monitoring system depending on the grid fault (described in the previous chapter). The MPPT and machine side controller are replaced by the dc-link voltage controller.

4.2. Control Design Under Balanced Grid Voltages

4.2.1. Maximum Power Point Tracking of PV

There are several methods for MPPT and the most common are [86]

1. Perturb & Observe (P&O)
2. Constant Voltage
3. Incremental Conductance

Among these methods, the incremental conductance method is recommended because it offers good yield under rapidly changing atmospheric conditions. The incremental conductance method measures the incremental change in the voltage and the current to predict the effect of a voltage change. It estimates the relationship between the operating point voltage, v_0, and the maximum power point voltage, v_{max} [86]. When light intensity and temperature change, the incremental conductance method controls the output voltage smoothly and reduces oscillation phenomena near the maximum power point (MPP) [87], [88].

The power across the PV array is given by

$$P_{pv} = v_o i_p \tag{4.1}$$

The MPPT algorithm follows the power variation

$$dP_{pv} = dv_o i_p + v_o di_p \tag{4.2}$$

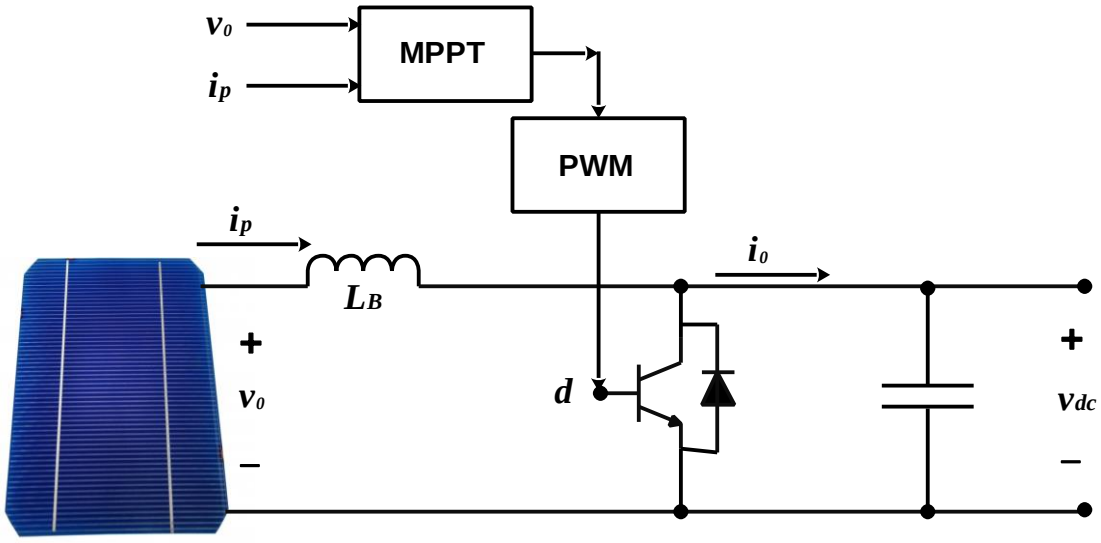

Figure 13 Photovoltaic side control scheme

At the maximum power point, the power variation with respect to the voltage is forced, by changing the duty cycle *d* of the dc-dc converter, such as

$$\frac{dP_{pv}}{dV} = i_p + v_0 \frac{di_p}{dv_0} = 0 \tag{4.3}$$

PV generator side control scheme is illustrated in Figure 13. The method can be expressed following the three conditions [89]:

$$\frac{di_p}{dv_0} = -\frac{i_p}{v_0}; \left(\frac{dP_{pv}}{dv_0} = 0 \right) \text{at MPP thus } v_0 = v_{max} \tag{4.4.a}$$

$$\frac{di_p}{dv_0} > -\frac{i_p}{v_0};\left(\frac{dP_{pv}}{dv_0} > 0\right) \text{ left of MPP thus } v_0 < v_{max} \quad (4.4.b)$$

$$\frac{di_p}{dv_0} < -\frac{i_p}{v_0};\left(\frac{dP_{pv}}{dv_0} < 0\right) \text{ right of MPP thus } v_0 > v_{max} \quad (4.4.c)$$

The flowchart of this algorithm is shown in Figure 14.

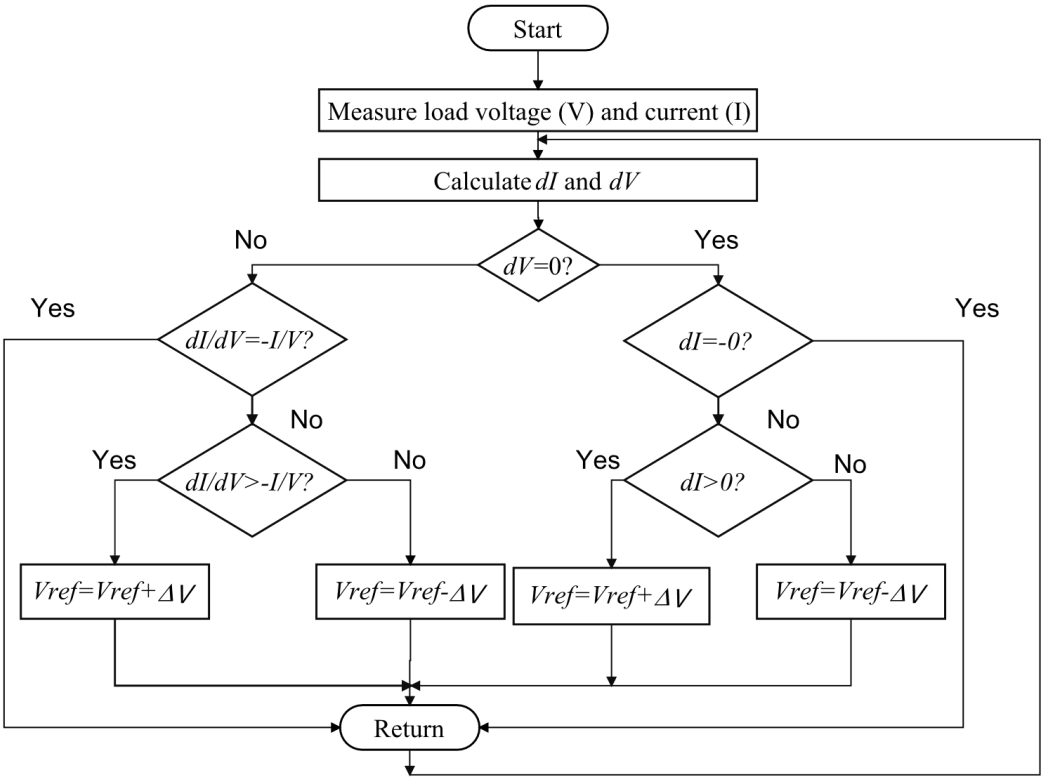

Figure 14 Flow chart of Incremental Conductance Method

4.2.2. Generator Side Control of the PMSG

The rotational motion dynamics of the wind turbine is expressed as

$$\dot{\omega}_r = -\frac{F}{J}\omega_r + \frac{1}{J}[T_r - T_e] \quad (4.5)$$

where T_e is the generator torque, T_r is the turbine torque, J is the total moment of inertia and F is total damping.

The generator torque is expressed by [90]

$$T_e = -p\phi_v\sqrt{3}\sin(\theta_e - \frac{\pi}{3})i_{\mathrm{p}} = -\Gamma i_{\mathrm{p}} \tag{4.6}$$

where θ_e is the electrical angle of the vector orientation, carried out from the rotational angular speed ($\theta_e = \int p\omega_r\, dt$), p is the pole pair number, and ϕ_v is the permanent magnet magnetic flux linkage.

The current dynamics of the boost dc-dc converter is expressed as [90]

$$\frac{di_{\mathrm{p}}}{dt} = -\frac{v_{\mathrm{dc}}}{L_b}\left[(d-1) + \frac{v_0}{v_{\mathrm{dc}}}\right] \tag{4.7}$$

where i_{p} is the converter input current, v_0 is the converter input voltage, v_{dc} is the converter output voltage (dc-link voltage), L_b is the converter inductance and d is duty signal of the switching signal.

The voltage dynamics, across the dc-link capacitor, has the following expression

$$\frac{dv_{\mathrm{dc}}}{dt} = \frac{1}{C}(i_0 - i_{\mathrm{dc}}) \tag{4.8}$$

where v_{dc} is the dc-link voltage, i_0 is the dc-dc converter output current, and i_{dc} is the inverter input current inverter, and C is the dc-link capacitance.

At both sides of the dc-dc converter, assuming ideal converter, the current relationship is given by

$$i_0 = (1-d)i_p \tag{4.9}$$

Therefore, using (4.9), the dc-link voltage dynamics (4.8) can be reorganized such as

$$\frac{dv_{dc}}{dt} = -\frac{i_p}{C}\left[(d-1) + \frac{i_{dc}}{i_p}\right] \tag{4.10}$$

where (d–1) can be considered as the control input in order to regulate the dc-link voltage through the dc-dc converter. This voltage dynamics will be used in the control scheme development under unbalanced grid voltages.

The wind generator side control system is developed from the rotational speed dynamics of equation (4.5)-(4.6) and the dc-dc converter current dynamics of equation (4.7). It has a cascade control loop:

1. An outer control loop that controls the rotational speed of the turbine-generator, to follow a reference speed generated by the MPPT algorithm, by using the rotor speed dynamics.
2. An inner control loop that regulates the current at the dc-dc converter using the current dynamics. The control strategies are based on proportional-integral (PI) regulators, and the wind generator side control scheme is illustrated in Figure 15.

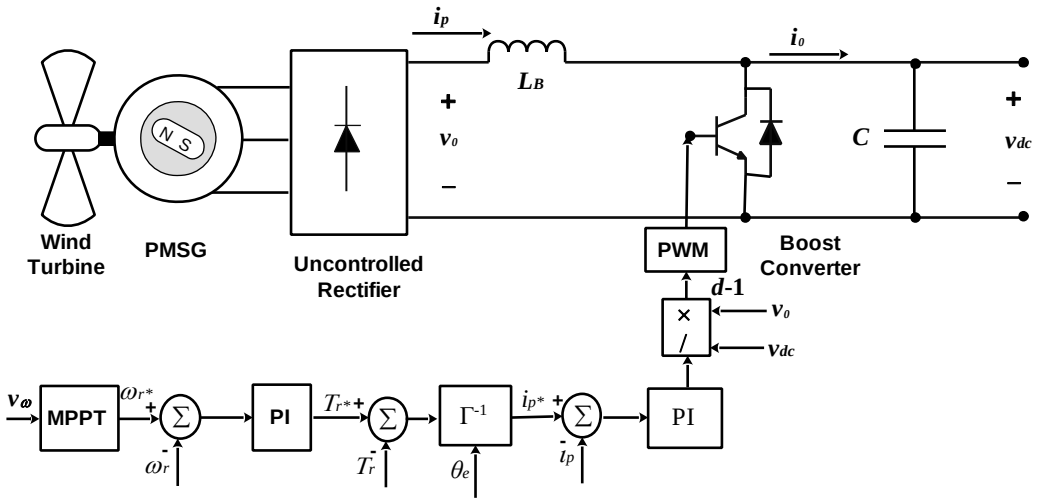

Figure 15 Generator side control scheme

4.2.1. Grid Side Control

The grid current dynamics is expressed using the *R-L* filter electrical equations and given by

$$\begin{cases} \dfrac{di_d}{dt} = -\dfrac{R}{L} i_d + \dfrac{1}{L}[L\omega i_q - e_d + v_d] \\ \dfrac{di_q}{dt} = -\dfrac{R}{L} i_q + \dfrac{1}{L}[-L\omega i_d - e_q + v_q] \end{cases} \tag{4.11}$$

where e_d, e_q, are the *d-q* component of the grid voltages, i_d, i_q are the *d-q* components of grid currents, v_d, v_q, are the *d-q* components of the inverter output voltages, ω is the grid frequency, *R* and *L* are the resistance and the inductance of the filter, respectively.

The active and reactive power, under balanced grid voltages, can be expressed, through orienting the *d-q* coordinates frame by e_q=0, as

$$\begin{cases} P = \frac{3}{2}(e_d i_d + e_q i_q) = \frac{3}{2} e_d i_d \\ Q = \frac{3}{2}(e_q i_d - e_d i_q) = -\frac{3}{2} e_d i_q \end{cases} \tag{4.12}$$

Assuming no power losses, the powers at the dc input and the ac-output of the inverter are equal, so

$$v_{\mathrm{dc}} i_{\mathrm{dc}} = \frac{3}{2} e_d i_d \tag{4.13}$$

The dc-link dynamics (8) can be reorganized using (4.13) to become

$$\frac{dv_{\mathrm{dc}}}{dt} = -\frac{3}{2}\frac{e_d}{C v_{\mathrm{dc}}} i_d + \frac{1}{C} i_0 = -\frac{3}{2}\frac{e_d}{C v_{\mathrm{dc}}}\left[i_d - \frac{2}{3}\frac{v_{\mathrm{dc}}}{e_d} i_0 \right] \tag{4.14}$$

where i_d can be considered as the control input in order to regulate the dc-link voltage through the inverter. This voltage dynamics will be used in the control scheme development under balanced grid voltages.

The grid side control system, for wind and PV systems, consists of a cascade control loop, as shown in Figure 16, where an outer control loop is used to regulate the dc-link voltage, using the voltage dynamics (4.14) and an inner control loop to regulate the currents, using the dynamics (4.11), in order to ensure the proper power transfer through the inverter. In order to achieve the unity power factor, the reference for *q* component of the grid current is taken as zero to ensure zero reactive power based on (4.12).

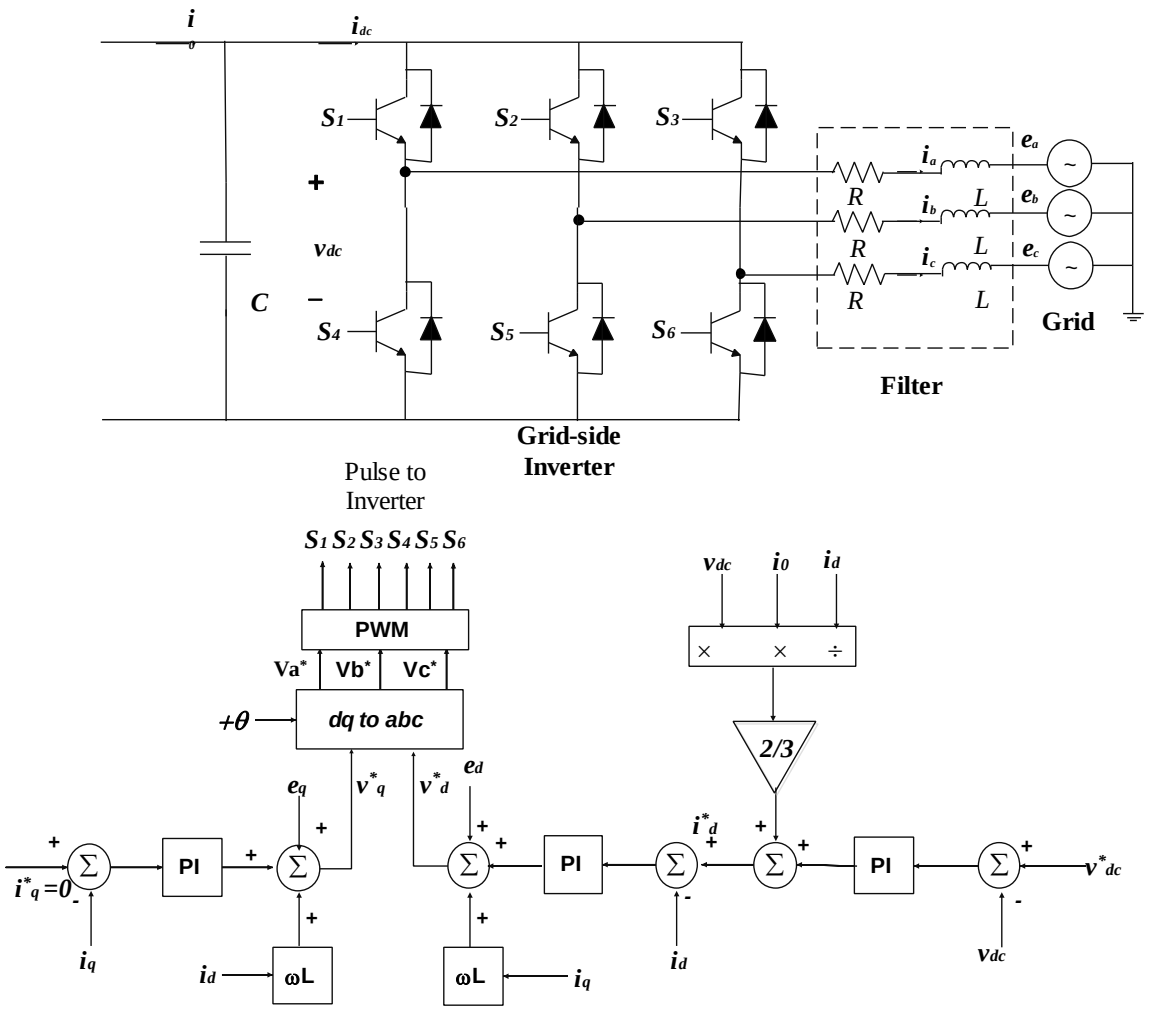

Figure 16 Grid side control scheme under normal grid operation

4.3. Control Design Under Unbalanced Grid Voltages

The instantaneous active and reactive powers, under unbalanced grid voltage, are expressed as [34]

$$\begin{cases} P = P_0 + P_c \cos(2\omega t) + P_s \sin(2\omega t) \\ Q = Q_0 + Q_c \cos(2\omega t) + Q_s \sin(2\omega t) \end{cases} \tag{4.15}$$

where P_0 and Q_0 are the average values of the instantaneous active and reactive powers, respectively, and P_c, P_s, Q_c, and Q_s are the oscillating terms, of second-order, in these instantaneous powers.

The power components (P_0 P_c, P_s, Q_0, Q_c, Q_s) are expressed with respect to positive and negative sequences of the voltages and currents, defined in synchronous reference frames ($(d, q)^+$ and $(d, q)^-$), such as

$$\begin{cases} P_0 = \frac{3}{2}(e_d^+ i_d^+ + e_q^+ i_q^+ + e_d^- i_d^- + e_q^- i_q^-) \\ P_c = \frac{3}{2}(e_d^- i_d^+ + e_q^- i_q^+ + e_d^+ i_d^- + e_q^+ i_q^-) \\ P_s = \frac{3}{2}(e_q^- i_d^+ - e_d^- i_q^+ - e_q^+ i_d^- + e_d^+ i_q^-) \end{cases} \tag{4.16}$$

$$\begin{cases} Q_0 = \frac{3}{2}(e_q^+ i_d^+ - e_d^+ i_q^+ + e_q^- i_d^- - e_d^- i_q^-) \\ Q_c = \frac{3}{2}(e_q^- i_d^+ - e_d^- i_q^+ + e_q^+ i_d^- - e_d^+ i_q^-) \\ Q_s = \frac{3}{2}(-e_d^- i_d^+ - e_q^- i_q^+ + e_d^+ i_d^- + e_q^+ i_q^-) \end{cases} \tag{4.17}$$

where $e_d^+, e_q^+, e_d^-, e_q^-$ are the positive- and negative sequences of the grid (d, q) voltages, $i_d^+, i_q^+, i_d^-, i_q^-$ are the positive and negative sequences of the (d, q) currents components.

Therefore, only four power components from (4.16) and (4.17) can be considered as the controlled outputs such as

$$\begin{bmatrix} P_0 \\ P_c \\ P_s \\ Q_0 \end{bmatrix} = \frac{3}{2} \begin{bmatrix} e_d^+ & e_q^+ & e_d^- & e_q^- \\ e_d^- & e_q^- & e_d^+ & e_q^+ \\ e_q^- & -e_d^- & -e_q^+ & e_d^+ \\ e_q^+ & -e_d^+ & e_q^- & -e_d^- \end{bmatrix} \begin{bmatrix} i_d^+ \\ i_q^+ \\ i_d^- \\ i_q^- \end{bmatrix} \tag{4.18}$$

The grid current dynamics, using the positive and negative sequences of voltages and currents, is expressed by

$$\begin{cases} \dfrac{di_d^{\pm}}{dt} = -\dfrac{R}{L} i_d^{\pm} \pm \omega i_q^{\pm} - \dfrac{e_d^{\pm}}{L} + \dfrac{1}{L} v_d^{\pm} \\ \dfrac{di_q^{\pm}}{dt} = -\dfrac{R}{L} i_q^{\pm} \mp \omega i_d^{\pm} - \dfrac{e_q^{\pm}}{L} + \dfrac{1}{L} v_q^{\pm} \end{cases} \tag{4.19}$$

where the positive and negative sequences of each quantity are $i_d^{\pm} = [i_d^+ \quad i_d^-]^T$, $i_q^{\pm} = [i_q^+ \quad i_q^-]^T$, $v_d^{\pm} = [v_d^+ \quad v_d^-]^T$, $e_d^{\pm} = [e_d^+ \quad e_d^-]^T$, $e_q^{\pm} = [e_q^+ \quad e_q^-]^T$

In the control system, the positive and negative-sequences current reference is calculated from (2.4), such as in order to track the reference tracking the selected active and reactive powers (P_0^*, Q_0^*).

$$\begin{bmatrix} i_d^+ \\ i_q^+ \\ i_d^- \\ i_q^- \end{bmatrix} = \frac{3}{2} \begin{bmatrix} e_d^+ & e_q^+ & e_d^- & e_q^- \\ e_d^- & e_q^- & e_d^+ & e_q^+ \\ e_q^- & -e_d^- & -e_q^+ & e_d^+ \\ e_q^+ & -e_d^+ & e_q^- & -e_d^- \end{bmatrix}^{-1} \begin{bmatrix} P_0^* \\ 0 \\ 0 \\ Q_0^* \end{bmatrix} \tag{4.20}$$

where, P_0^*, Q_0^* are the references for the injected active and reactive powers during the voltages unbalance, and the zeros are for canceling the active power oscillations term (P_c, P_s).

In the operation of the renewable (wind, PV) energy conversion systems under abnormal grid conditions (voltage dip), the objectives are:

1. Regulation of the dc-link voltage, to be maintained constant, by the dc-dc converter using the generator side control system.

2. Injection of the active and reactive powers, to support the grid and meet LVRT requirements, which is conducted through the inverter using the grid side control system.

4.3.1. Generator Side Control

The dc-link voltage regulation is performed using the voltage dynamics (4.14) and a PI controller to provide the duty cycle to the dc-dc converter. The control scheme, for wind and PV systems, is shown in Figure 17.

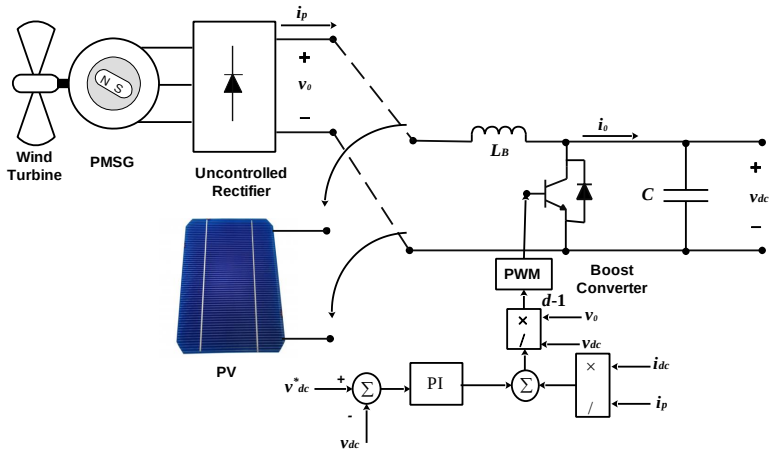

Figure 17 Generator side control scheme under grid fault

4.3.2. Grid Side Control Under Grid Fault

The grid side control system consists of controlling the *d-q* components of the grid currents, using the dynamics 4.19, to track references carried out from the injected active and reactive powers by 2.8. It has a dual-frame control structure, where one controller is used for the positive sequence and the other for the negative sequence, and the command is the sum of both sequences as shown in Figure 18.

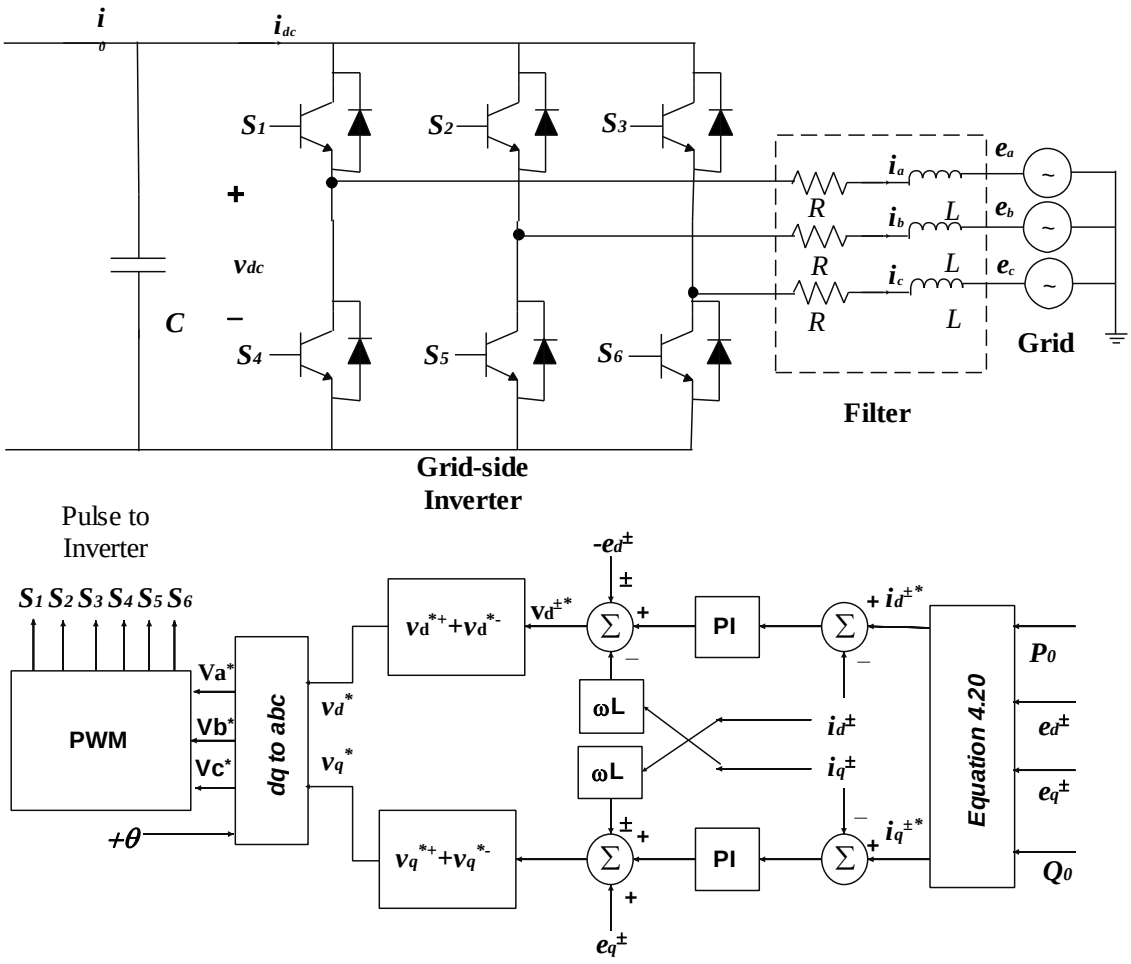

Figure 18 Generator side control scheme under grid fault.

4.4. Conclusion

This chapter gives a details description of the control system design of the grid-connected PV and wind power system. The control system has two modes; normal grid condition (mode I) and grid fault condition (mode II). In mode I, the dc-dc converter is controlled in order to achieve maximum power extraction whereas the inverter is controlled to maintain a constant dc-link voltage and power transfer at a unity power factor. In mode II, the dc-

link voltage regulation is achieved by the dc-dc converter and the required active and reactive powers injection are achieved by the inverter to meet the grid code requirements.

Chapter 5: Experimentation and Result

5.1. Introduction

Real-time simulation is defined as a computer model of the physical system that runs at the same rate as the actual physical system [91]. It is very useful to test and detect any design faults of the system at an early stage, thereby decreasing design costs [92].

Real-time simulation can be divided broadly into three types [91], [93].

1. Rapid control prototyping (RCP)
2. Hardware-in-Loop (HIL)
3. Pure Simulation (PS)

In rapid control prototyping application, a real-time simulator implements a plant controller model and connects to a physical system via input and output ports of the simulator. On the other hand, HIL is used to test a real controller connected to simulated plant model. In PS application, a real-time simulator simulates both the controller model and the plant model [91], [93].

In this chapter, a brief description of the experimental system is demonstrated. It includes system configurations and working procedures involve in the proposed system. Finally, the experimental result of the proposed system is presented with the real working scenario.

5.2. System Description of the Real-Time Simulation

5.2.1. Real Time Simulator

The real-time digital simulator (OP56000) is a complete simulation system comprising a powerful computer, a flexible high-speed front-end processor, and a signal conditioning stage. It consists of analog and digital I/O signal modules, a multi-core processor and FPGA that runs RT-LAB real-time simulation software platform. It is equipped with the processor Intel Xeon Quad Core 2.40 GHz, which makes it a powerful tool for RCP and hardware-in-the-loop (HIL) applications [22], [94]. It has a different set of digital and analog I/O ports to interface with the external system. The OP5600 gives access through RJ45 connectors to a large array of digital and analog IO's. Signals coming from the RJ45 connectors can be routed into mini-BNC outputs (up to 16 channels) that can be monitored by oscilloscopes.

5.2.2. RT-LAB Software

The RT-LAB software represents integrates an Opal-RT real-time simulator (OP5600) with the powerful graphical and model-based Matlab/ Simulink software [95]. The process of running Simulink model in the OP5600 simulator is illustrated in Figure 19.

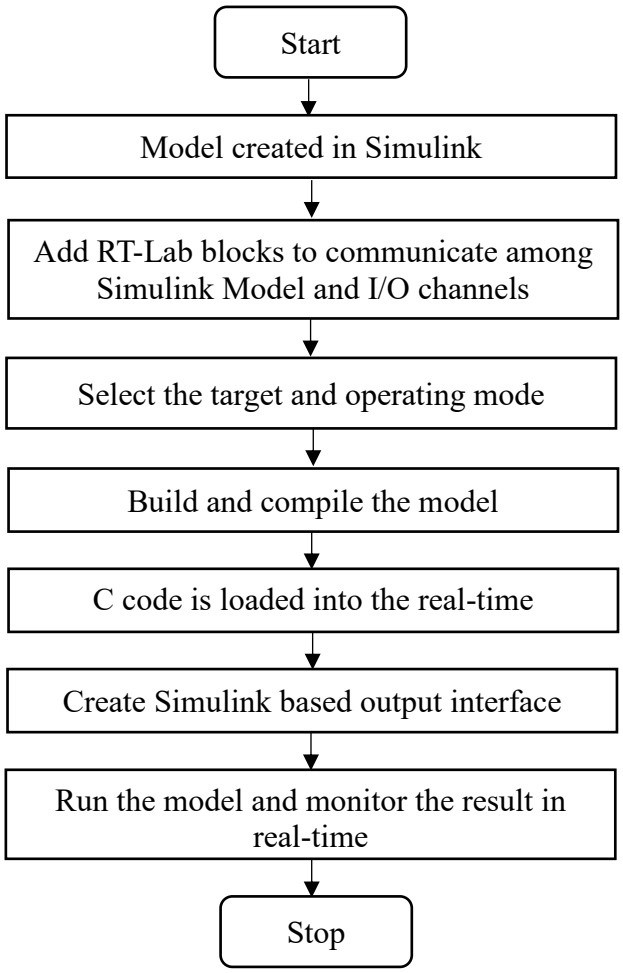

Figure 19 Flow diagram of model execution in the RT-Lab software

At first, a model is created in Simulink. In order to run the Simulink model in the RT-Lab, there are specific RT-Lab blocks. These RT-Lab blocks communicate among Simulink model and I/O channels. The specific target and operating mode are selected based upon operating mode. The model is then built and compiled in RT-Lab software. A C code is generated and loaded to the real-time simulator once the building and compiling are successful. Then, a new Simulink output interface is created automatically. After running the model, the model is operating in real-time and showing the output in the console panel. Finally, the model is stopped after observing the output.

5.2.3.Rapid Control Prototyping in the RT-Lab

All Simulink model can be implemented in the RT-Lab environment by following specific steps. The block diagram of the Simulink model must be modified by regrouping the model into subsystems and inserting OpComm blocks [94].

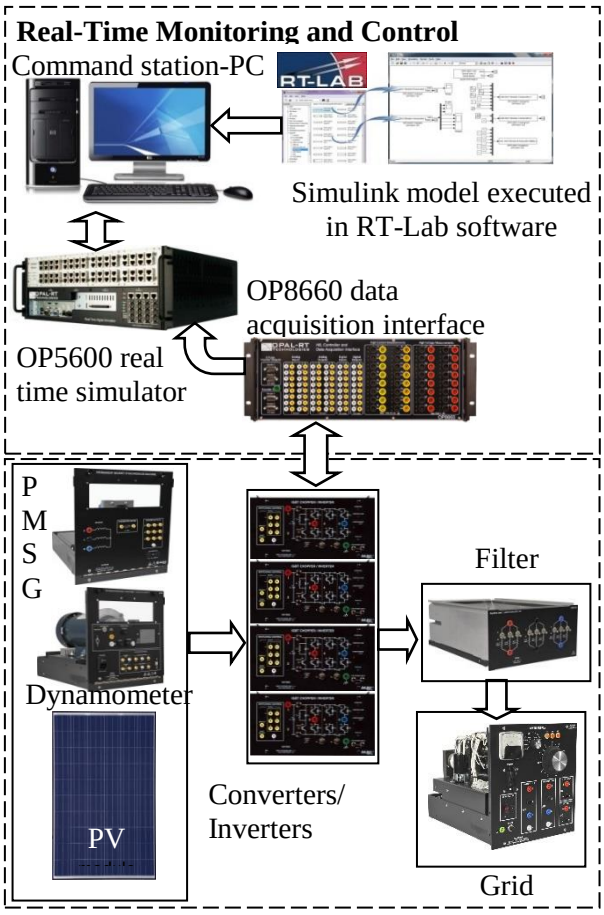

Figure 20 Real-time system for the HIL for grid-connected PV-wind hybrid system

In RT-Lab, all the subsystems must be named with two prefixes based upon their function. The prefixes are console subsystem (SC_) and master subsystem (SM_). There is at least one OpComm block in the console subsystem (SC_). It contains all user interface blocks

including scopes, displays, switches that run asynchronously from the other subsystems. Each master subsystem in RT-Lab is represented by a core that performs its processes in the efficient and fast way. In the RT-Lab model, there must be at least one master subsystem in each model. The master subsystem (SM_) contains all the computational elements of the model, the mathematical operations, the input and output blocks, and the signal generators. After grouping the model, OpComm blocks must be added to enable and save communication setup data. All inputs of subsystems must first go to OpComm block before being used. The RCP of grid-connected PV/wind system is shown in Figure 20. After connecting input/output hardware, the Simulink model is compiled in RT-Lab. Then, it is loaded in OP5600 real-time simulator for the master subsystem. Finally, all the subsystems are executed by OP5600 simulator.

5.3. Experimental Set-up

Two separate grid-connected renewable energy conversion systems are proposed in the research work: PV and wind power system. The experimental grid-connected PV power system is shown in Figure 21. It consists of the PV array, dc-dc converter, inverter, resistive-inductive filter, and a three-phase power supply to emulate the grid. The properties of these elements are provided in the Appendix. The irradiance is manipulated through five industrial lamps, where full irradiance means that the five lamps are ON.

On the other hand, the experimental grid-connected wind power system consists of a four four-quadrant dynamometer to emulate the wind turbine, a PMSG coupled with a dynamometer, three IGBT/Chopper modules, a power supply to emulate electric grid, a

line inductor filter. The system parameters are listed in the appendix A. The experimental grid-connected wind power system is shown in Figure 22.

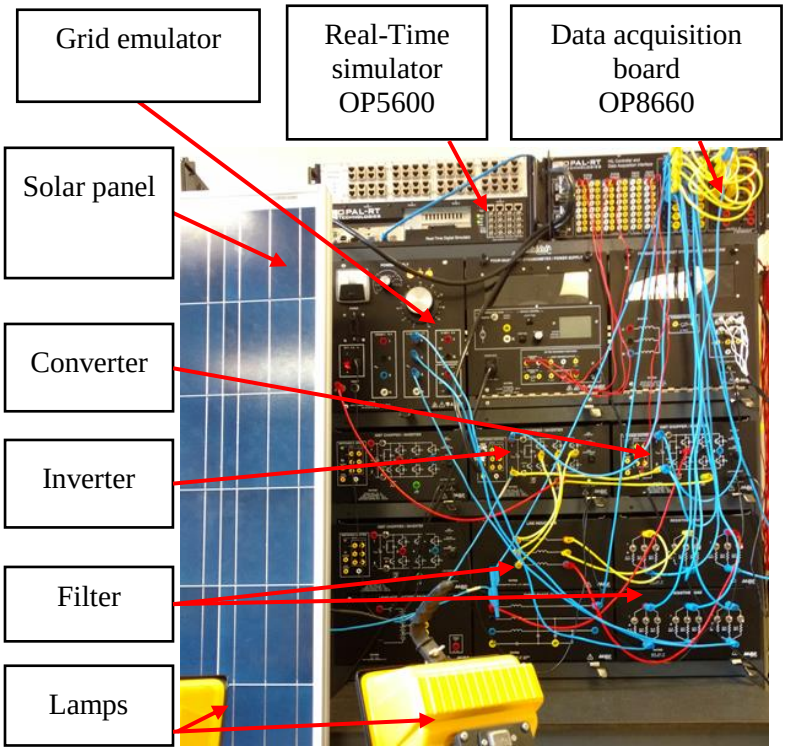

Figure 21 Experimental three-phase grid connected PV system

The speed of the wind turbine is changed by the LVDAC software integrated with the dynamometer. The software interface of the wind turbine is shown in Figure 23. The speed, gear ratio, pulley ratio can be changed easily from the software. It has a package of control functions that can be activated in the four-quadrant dynamometer enabling the module to emulate the operation of a real wind turbine. For the both experimental set-up, the voltages and the currents were measured by the data acquisition interface (OP8660). The proposed control system was built in Simulink and run in the OPAL-RT real-time simulator (OP5600) through the software RT-LAB [94], [96].

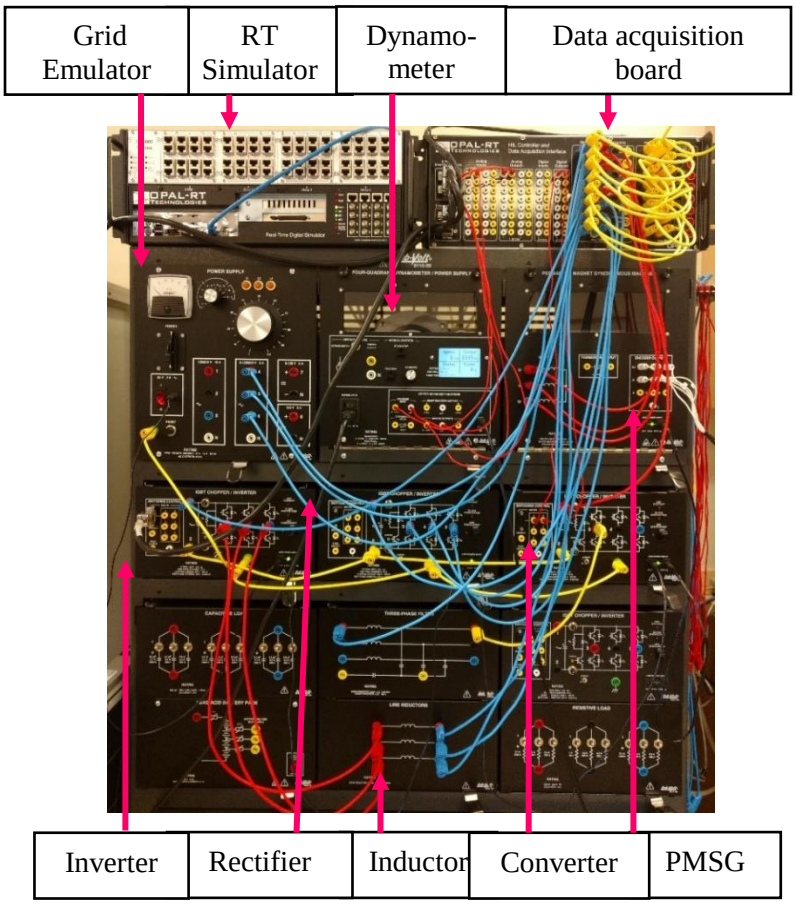

Figure 22 Experimental set-up for the three-phase grid-connected wind power system

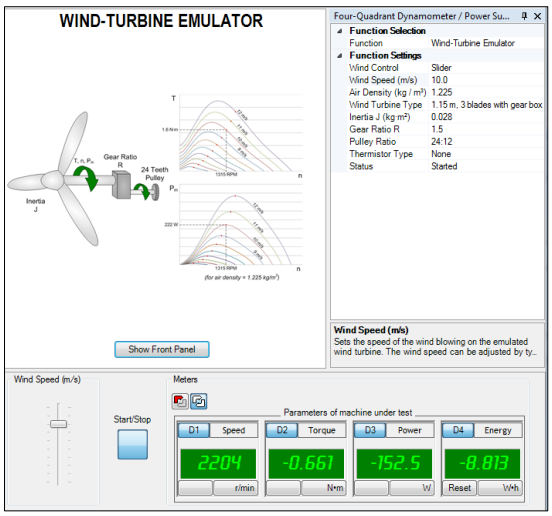

Figure 23 The LVDAC software interface of the wind turbine emulator

5.4. Experimental Result

Four cases have been considered demonstrating the operation and performance of the proposed system. The grid fault was manually accomplished through changing simultaneously the three-phase voltage of the power supply. From the voltage dip calculation, it can be noticed that the control system will behave similarly in balanced and unbalanced voltage dips as only the minimum value of the phase voltage will be used in the voltage dip computation. The control gains were chosen by trial and error technique and kept constant in all experimental cases for each system. The control gain of the PV and wind power system are listed in the Appendix.

5.4.1. Photovoltaic Energy Conversion System

Case 1: Dual-mode operation under constant dc-link voltage reference and constant irradiance

In this experiment, the PV system is tested under full irradiance and constant dc-link voltage reference. The zoomed grid voltage is shown in the top of Figure 24. A voltage dip occurs after t=20s and ends after t=30s as shown in Figure *24.a* from the grid voltage and in Figure *24.b* for the voltage dip detected by the grid fault monitoring system. It can be observed that the dc-link voltage is successfully regulated to follow the constant reference with a smooth transition between the modes, as shown in Figure *24.c*, where a small voltage peak occurs at the transition from Mode II to Mode I, as the voltage controller of Mode I have a direct effect on the grid inverter, but rapidly eliminated by this controller to follow the constant reference. This peak phenomenon does not occur in the transition between

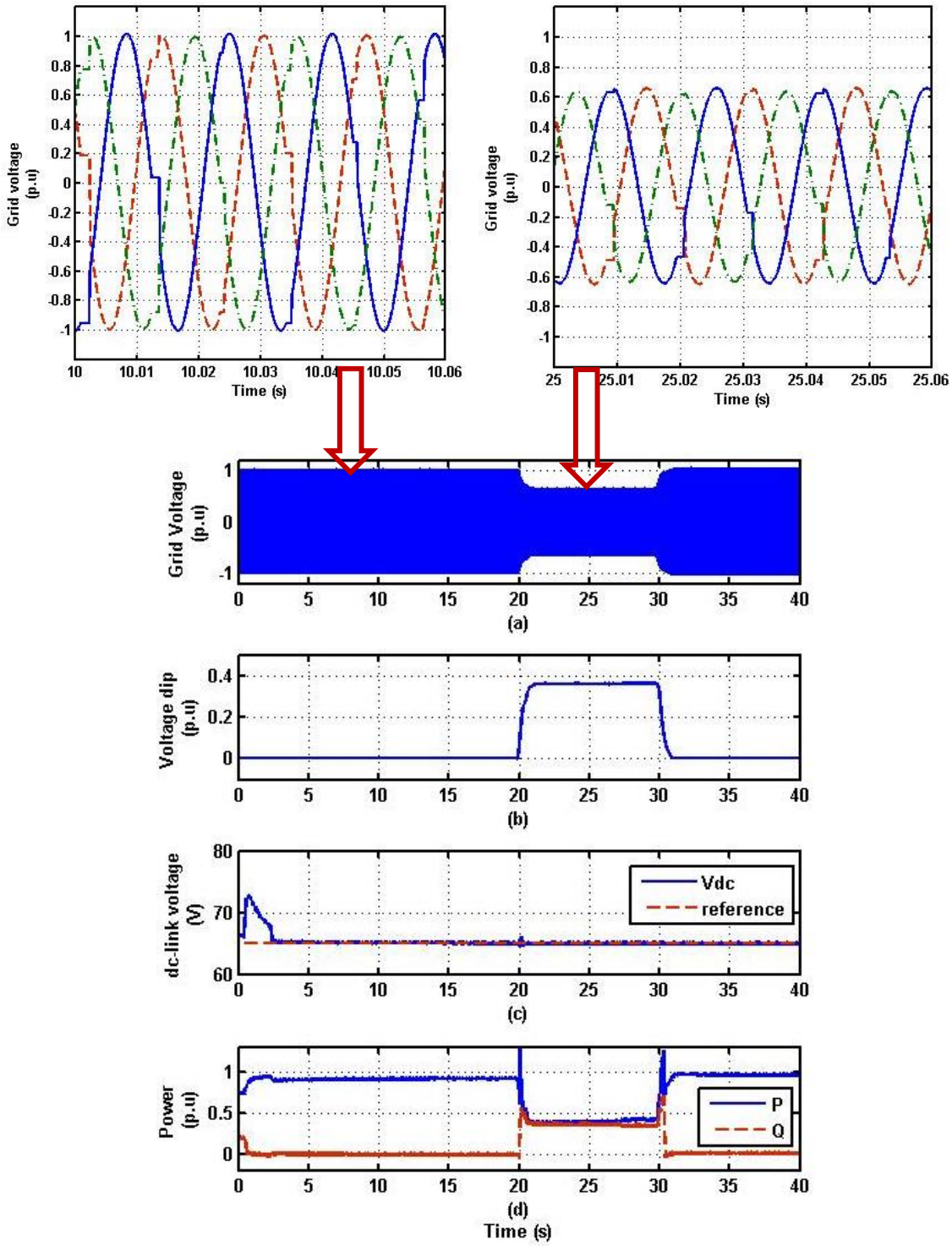

Figure 24 Operation under constant dc-link voltage and constant irradiance. (a) grid voltage, (b) voltage dip, (c) dc-link voltage regulation, (d) active and reactive power

Mode I and II because the voltage controller in Mode II provides the pulses to the PV side dc-dc voltage, which is indirectly connected to the grid through the inverter. At the start, the harsh transient regime, in the dc-link voltage, is due to the state of the dc-link capacity. The power response is shown in Figure *24.d*, where the active and reactive power follows constant and null references respectively.

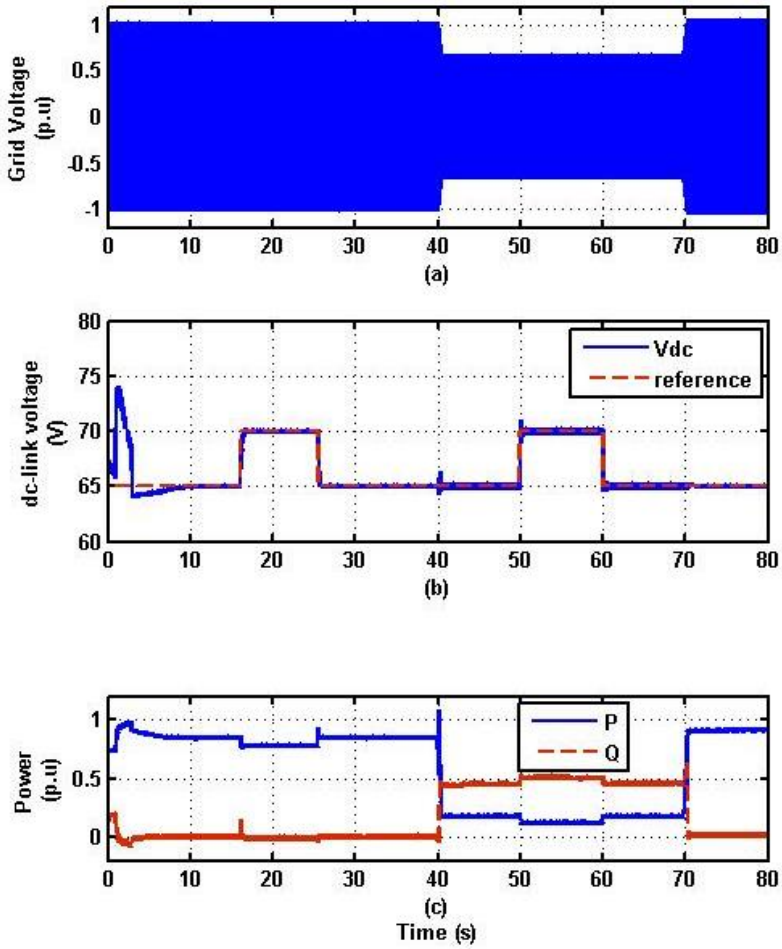

Figure 25 Operation under variable dc-link voltage and constant irradiance. (a) grid voltage, (b) dc-link voltage regulation, (c) active and reactive power

Case 2: Dual-mode operation under variable dc-link voltage reference and constant irradiance

Now, the proposed control strategy is tested for operation under a variable dc-link voltage reference while maintaining the irradiance constant. Grid voltages, shown in Figure *25.a*, are applied to simulate modes I and II, and in each mode, the voltage reference is changed to evaluate the tracking performance. From Figure *25.b*, it can be observed that the voltage tracking occurs with a fast response to the changes of the reference. Also, the control switching between mode I and mode II occurs without influence on the dc-link voltage response, which demonstrates the high performance of the proposed control system.

Case 3: Dual-mode operation under constant dc-link voltage reference and variable irradiance

In this case, the robustness of the proposed control system is tested under changing irradiance condition. This variation is done through turning ON limited number of lamps at different time instants (three lamps ON until t=15s; from t=15s to t=35s, five lamps ON; from t=35s to t=42s, three lamps ON; from t=42s to t=50s, three lamps ON; and from t=50s to t=60s, five lamps ON), and can be seen in the PV voltage response of Figure *26.a*. The voltage dip is illustrated in Figure *26.b*. From Figure *26.c*, it can be observed that the dc-link voltage is successfully regulated despite the changes in the irradiance and the power responses are successfully following the conditions of modes I and II as shown in Figure *26.d*.

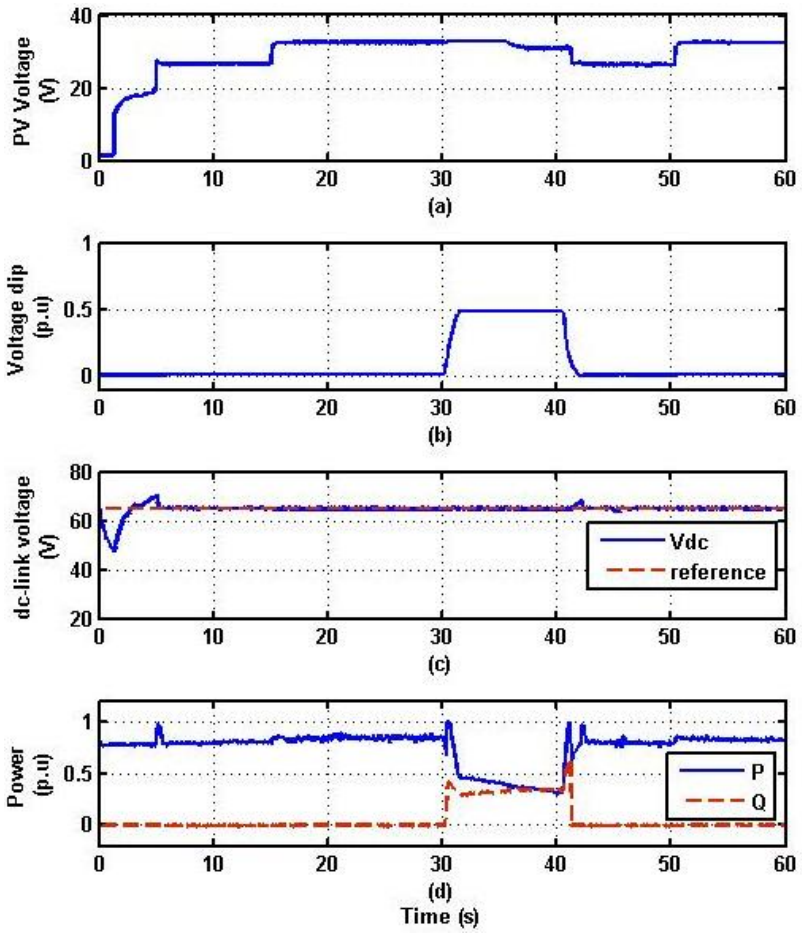

Figure 26 Operation under constant dc-link voltage and variable irradiance. (a) PV voltage, (b) voltage dip, (c) dc-link voltage regulation, (d) active and reactive power

Case 4: Dual-mode operation under parametric uncertainties

In order to deal with another issue of robustness, the control system was tested under parametric uncertainties by changing the values of the parameters in the control laws (50% increase in the inductance *L* and 50% decrease in the resistance *R*). The grid fault is characterized by the voltage dip shown in Figure *27.a* and *27.b*. The dc-link voltage regulation, under nominal value and perturbed value of (*R*, *L*) is shown in Figure *27.c*, where it can be observed that the voltage response follows the constant reference without

any influence from the parameters. Furthermore, the power responses concur with the references to normal and fault conditions, as shown in Figure *27.d.*, despite the parametric changes. These results demonstrate the robustness of the control system to parametric uncertainties.

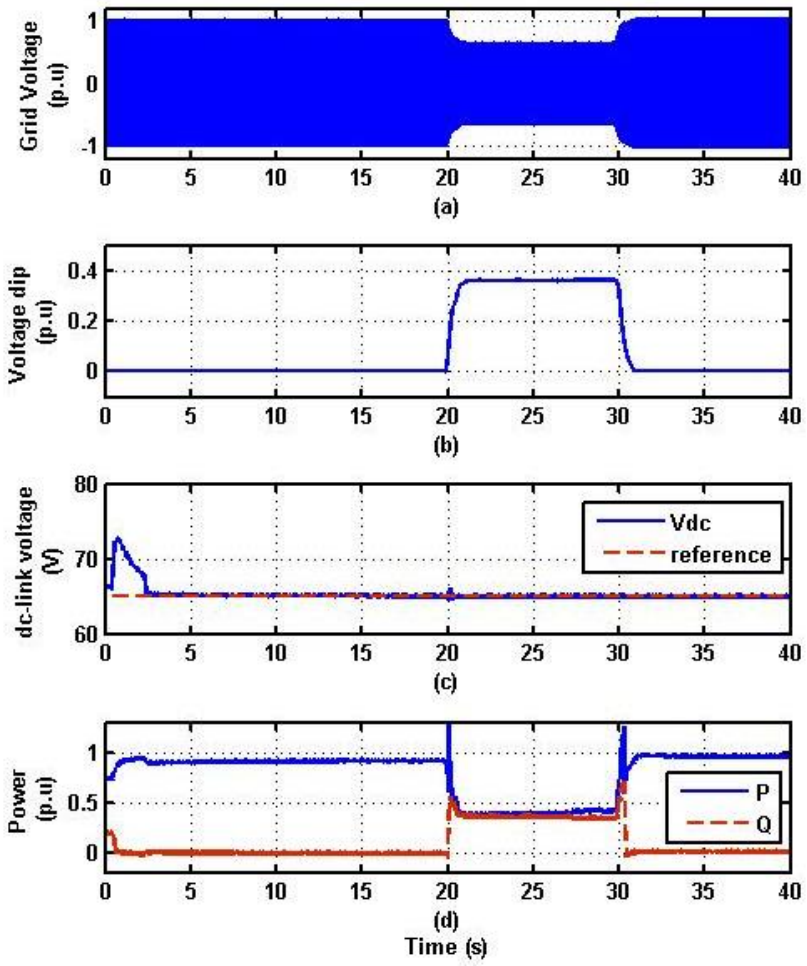

Figure 27 Operation under parametric uncertainties. (a) grid voltage, (b) voltage dip, (c) dc-link voltage regulation, (d) active and reactive power

5.4.2.Wind Energy Conversion System

Case 1: Operation under constant wind speed and constant dc-link voltage

In this experiment, the proposed control scheme is tested under grid voltages, shown in Figure *28* and *29.a*, where the fault occurs at t=20s.

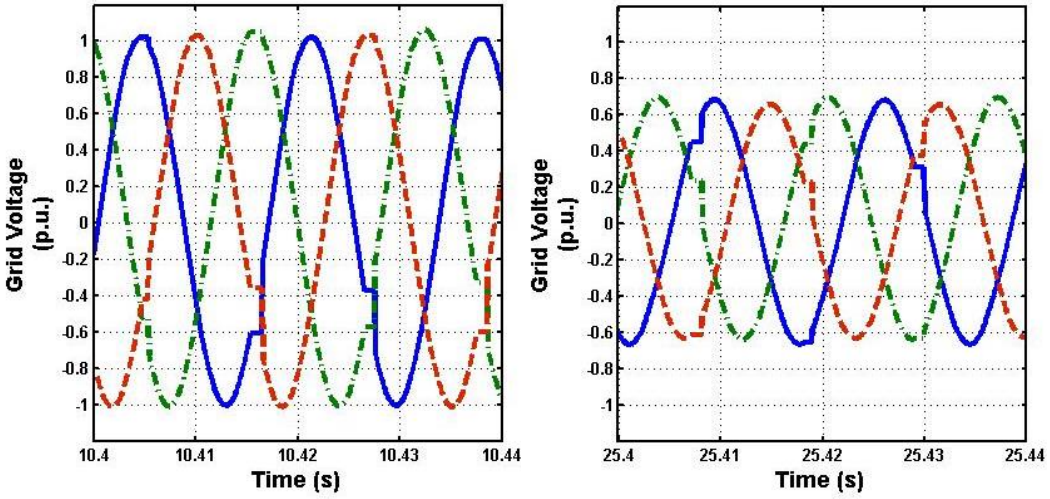

Figure 28 Grid voltage (a) normal, (b) grid fault

The rotational speed, shown in Figure *29.b*, is constant and the dc -link voltage, shown in *Figure 29.c;* is successfully regulated to track the constant voltage reference. It can be observed that the dc -link voltage remains constant despite the transitions, occurring at t=20s and t=30s, due to the balanced and unbalanced grid voltages and the difference dc -link voltage control systems. Furthermore, the active and reactive power responses, shown in Figure *29.d*, concur with the power requirement. In the case of balanced grid voltages, the active power follows the rotational speed profile, to extract the maximum power from wind, and the reactive power is regulated to be zero to ensure unity power factor. In the case of unbalanced grid voltages, the active power is curtailed, to ensure limited current,

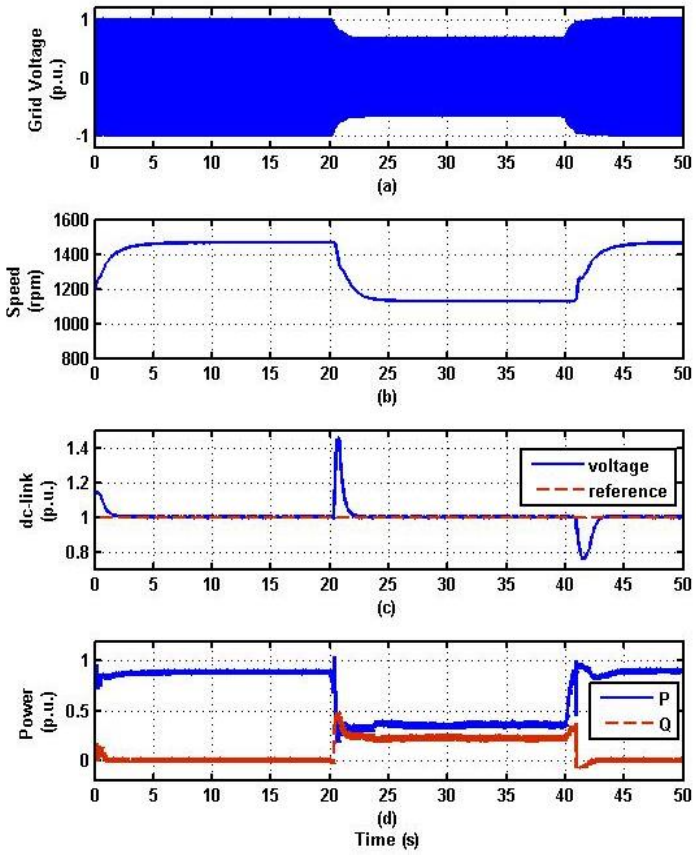

Figure 29 Operation under constant dc-link voltage and constant irradiance.

(a) grid voltage, (b) wind speed, (c) dc-link voltage, (d) power

and the reactive power is injected according to the condition (2.4). These results demonstrate the effectiveness of the proposed control system to operate the WECS in both regions of grid voltages.

Case 2: Operation under constant wind speed and variable dc -link voltage

In order to verify the voltage tracking performance in normal and grid fault conditions, shown in Figure 30.*a*, the voltage profile was changed, as shown in Figure *30.c*, where it can be observed that fast tracking is obtained in all conditions. The power responses are

illustrated in Figure *30.d*, where it can be observed that the active power is affected by the dc-link link voltage change in normal operation while the injected reactive power relies on the maximum current tolerated by the inverter in case of grid fault.

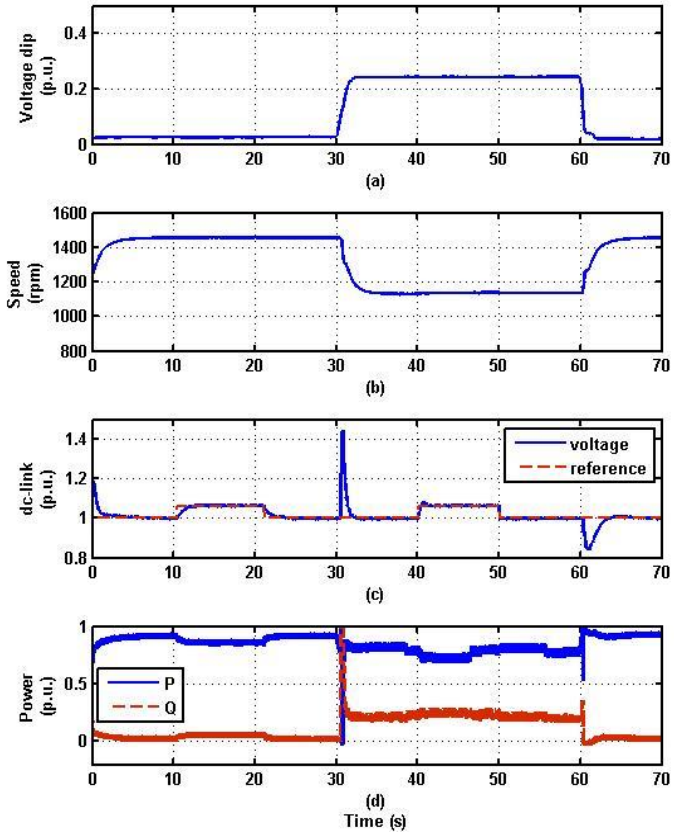

Figure 30 Operation under variable dc-link voltage and constant speed.

(a) voltage dip, (b) wind speed, (c) dc-link voltage, (d) power.

Case 3: Operation under variable wind speed

Figure *31* verifies the voltage tracking performance of proposed system in normal and grid fault conditions. In this case, the wind speed is changed in normal and faulty conditions as shown in Figure *31.b* where it can be observed that fast tracking is obtained in all

conditions. The power responses are illustrated in Figure *31.d*, where it can be observed that the active power is affected by the speed variation where reactive power remains constant in normal condition. In the faulty mode, the real and reactive power changes in accordance with the fault.

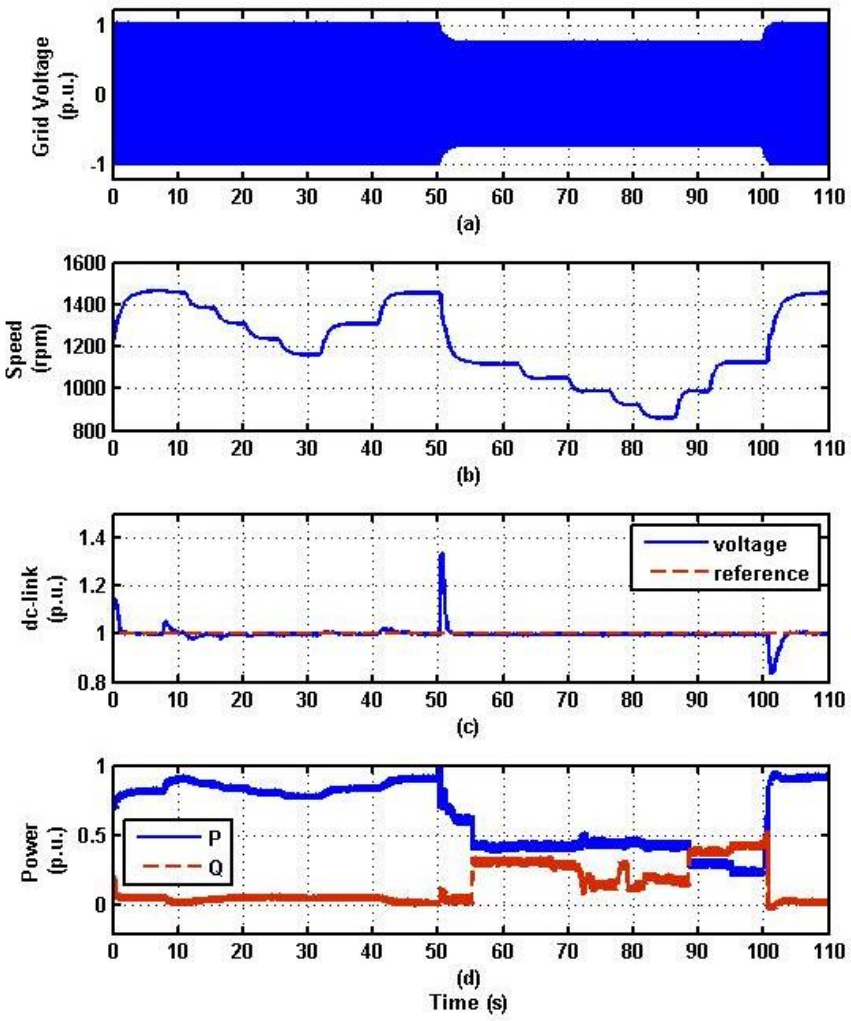

Figure 31 Operation under variable speed

(a) Grid voltage, (b) wind speed, (c) dc-link voltage, (d) power

Case 4: Operation under external Disturbance

The robustness of the proposed system to external disturbance was tested under adding line resistor and changing its value during operation which is shown in Figure *32*. a disturbance is created from 15s to 20s in mode and 45s to 50s in mode two. The dc-link voltage remains constant. It shows the robustness of the proposed system.

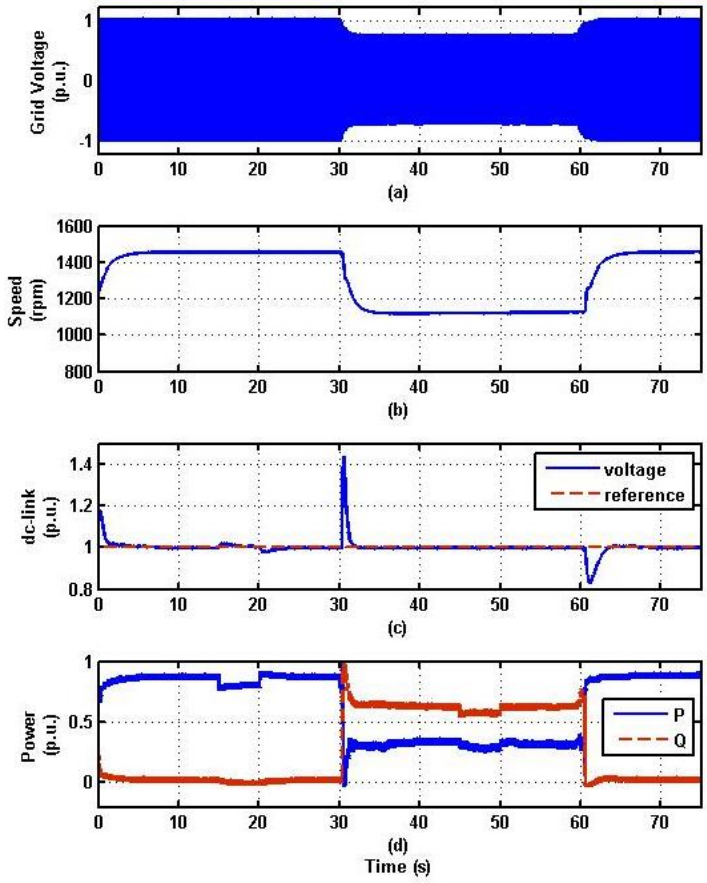

Figure 32 Operation under external disturbance

(a) Grid voltage, (b) wind speed, (c) dc-link voltage, (d) power

5.5. Conclusion

This chapter discusses the experimental system and experimental results. The proposed system is verified by the Opal-RT rapid control prototyping system. The system description and operating principle are described in detail. The experimental results are presented separately for the both PV and wind system. Both systems consider a real working scenario in order to verify the proposed system.

Chapter 6: Conclusion and Future Work

6.1. Conclusion

In this research work, a control interface of the grid-connected PV and wind power system are designed and practically implemented in the laboratory with a view to injecting real and reactive power in accordance with grid code requirements. The research work involves design and implementation of a control system and a grid fault monitoring system. The implemented grid connected PV and wind system can operate in both normal and faulty mode. The normal mode is operated with MPPT and the faulty mode is operated with the real and reactive power supply to the grid. The grid fault monitoring system detects the fault and switches the mode automatically. The controller for the faulty condition is designed in such a way that the inverter current never exceeds the current rating of the inverter to protect it during a grid fault. In addition, the real and reactive power references in faulty mode are based on the grid voltage sag conditions and maximum current rating of the inverter. A dual current controller is designed for controlling positive and negative sequence components under grid fault in order to deal with the asymmetrical faults. It permits the injection of the reactive current to the grid according to the reactive current requirement of grid codes in symmetrical and

asymmetrical grid faults. The effectiveness of the control scheme has validated been experimentally by testing different real working scenario.

6.2. Future Work

The present research work can be extended further. The opportunities for future work include the following

- Implementation of advanced control system such as Fuzzy logic, neural network, predictive controller to improve the performance of the system
- Integration of a battery to supply real/reactive power when renewable power is less than reference power obtained from fault monitoring system
- Testing the system in real grid fault condition

Appendix

A. System Specifications

Table 2 Specifications of CS6P-260M PV module under test conditions

Maximum Power (W)	260
Open Circuit Voltage (V)	37.8
Maximum Power Point Voltage (V)	30.7
Short Circuit Current (A)	8.99
Maximum Power Point Current (A)	8.48

Table 3 Parameters of the emulated wind turbine

Number of blades	3
Air density (kg/m^2)	1.225
Diameter (m)	1.15
Pulley ratio	24:12
Moment of inertia-J_r($kg \cdot m^2$)	0.028

Table 4 Parameters of the permanent magnet synchronous generator

Rated power (W)	260
Rated current (A)	3
Stator resistance-R_s (Ω)	1.3
Stator *d*-axis inductance- L_d (mH)	1.5
Stator *q*-axis inductance- L_q(mH)	1.5
Flux linkage ϕ_v - (Wb)	0.027
Number of pole pairs- p	3
Moment of inertia-J_g(kg·m^2)	1.7×10^{-6}
Coefficient of friction-K_g (Nm·s/rad)	0.314×10^{-6}

Table 5 Parameters of the DC bus and grid filter for the grid-connected photovoltaic

DC link voltage (V)	65 V
DC-link capacitor-C (mF)	1.8
Filter resistance-R (Ω)	0.5
Filter inductance- L (mH)	25

Table 6 Parameters of the DC bus and grid filter for the grid-connected wind power

DC link voltage (V)	85 V
Dc-link capacitor-*C* (mF)	1.8
Filter resistance-*R* (Ω)	0.5
Filter inductance- *L* (mH)	25

Table 7 Parameters for the emulated grid

Nominal voltage (V)	45
Frequency (Hz)	60

B. Controller Parameters

Table 8 Controller Parameter for the grid-connected photovoltaic

Mode I	Voltage controller k_p, k_i	400, 0.001
	Current Controller k_{pd}, k_{id}, k_{pq}, k_{iq}	0.6, 0.5, 0.6, 0.5
Mode II	Voltage controller k_p, k_i	0.2, 100
	Power Controller k_{pd}, k_{id}, k_{pq}, k_{iq}	0.3, 1, 0.3, 1

Table 9 Controller Parameter for the grid-connected wind power

Mode I	Speed Controller	0.001, 0.1
	Voltage controller k_p, k_i	500, 0.1
	Current Controller k_{pd}, k_{id}, k_{pq}, k_{iq}	0.8, 0.7, 0.8, 0.7
Mode II	Voltage controller k_p, k_i	0.1, 0.3
	Power Controller k_{pd}, k_{id}, k_{pq}, k_{iq}	5, 1, 5, 1

C. Steps required for executing Simulink model in RT-Lab

The following steps are required to start simulation using RT-Lab

1. Connect the OP5600 simulator to the OP8660 as shown in section 3.1 in the hardware user guide of High-Performance Real-Time Simulation and HIL Test Systems [93].
2. Connect the OP5600 simulator with the host computer as shown in section 3.2 in the hardware user guide.
3. Turn ON the OP5600 Real-time Digital Simulator.
4. Open RT-LAB in the host computer.
5. Make sure the 'Targets' in 'Project Explorer' window is connected with *LCSM*. To update the connection status, right click on the target *LCSM* and click *Refresh*. In the case of failure to connect, check the blue LAN/Network cable.
6. Create a new RT-LAB Project or access an existing RT-LAB Project (i.e. TEST).
7. Minimize RT-LAB, copy the required basic files, create a new folder (i.e. Control) in the following directory and paste all the files;

Local Disk (C:) > Users> Professor Adel > workspaces > TEST > models > Control

The folder must contain the Simulink model (.mdl) file named *HRES.mdl*, one (.bin) file and one (.conf) file. Both *.bin* and *.conf* files are required to define how the data acquisition read/write channels are assigned. Rename the file if required.

8. To import Simulink model, double-click on the project, right click on *Models*, go to *Add* select *Existing Model*. From the window click *Import* and select the file from the same directory where the model file (.mdl) was pasted before.

Local Disk (C:) > Users> Professor Adel > workspaces > TEST1 > models > Control

9. Open the RT-LAB window and select the imported file on the project.
10. To apply new control algorithm and modify/update the model, right click on the Simulink model, go to *Edit with* and select *Matlab R2011B (32bit) 7.13.* A new Matlab/Simulink window will appear to apply different control schemes and update the model as desired.
11. Perform the connection depicted between the OP8660 signal conditioning module and Lab-Volt's hardware. Make sure that the plugs of the DB9-8245 encoder cable are correctly connected to their corresponding encoder outputs on the front panel of the 8245 module.
12. Make sure that the selected converters and the PMSM module are fed through its 24V DC input,. Turn ON the selected inverter.
13. Turn ON the power input for the 8960-20 Dynamometer and make sure the USB cable is connected to the host computer.
14. Open LVDAC-EMS software from the start menu. Select the network voltage and frequency, 120V-60Hz, and then click *Ok.*
15. A new LVDAC-EMS window appears, from the *Tool* menu select *Four-Quadrant Dynamometer/Power Supply.*

16. To run the 8960 Dynamometer as an Emulator, the modification is required in the *Function Settings*, change the *Function* to *Wind-Turbine Emulator* and change *Function Setting*.
17. Save the model after modifying/updating, check the *Development* tab in RT-LAB and make sure that the *Target Platform* is set to *Redhat* for the selected Simulink model.
18. Check the *Execution* tab and make sure that the *Real-time Simulation Mode* is set to *Hardware Synchronized.*
19. To compile the simulation model, click on *Build*, make sure the proper Simulink model is selected for compilation.
20. Click on the *Assignation* tab and make sure that the Extra High Performance (XHP) mode in ON. Check the box to turn ON the XHP mode.
21. To upload the model in the real-time simulator, click *Load*. Errors may appear while loading, look for the error description in the *Display* tab and load again after correcting them.
22. If the model is successfully loaded a monitoring console will appear automatically in a new Matlab/Simulink window. The console can be identified by a yellow note titled as *'Automatically generated by RT-LAB during compilation'.*
23. Click *Execute* to run the model.
24. From the LVDAC console use slider to run the system with variable speed. The user console will allow the user to modify the references of the machine during the operation.

References

[1] *Key World Energy Statistics 2015*. International Energy Agency, 2015.

[2] (2017) Canada's Emission Trends 2014. [Online]. Available: https://ec.gc.ca/ges-ghg/default.asp

[3] (2017) World Bank Open Data. [Online]. Available: http://www.worldbank.org/en/topic/energy

[4] *World Energy Outlook 2015*. International Energy Agency, 2015.

[5] (2017) Climate Change Conference COP21. [Online]. Available: http://www.cop21paris.org/about/cop21.

[6] M. A. Islam, A. Merabet, R. Beguenane, H. Ibrahim, and H. Ahmed, "Simulation based study of maximum power point tracking and frequency regulation for stand-alone solar photovoltaic systems," in *International Conference on Renewable Energies and Power Quality (ICREPQ'14)*, Jan. 2014, pp.1-6.

[7] R. Akikur, R. Saidur, H. Ping, and K. Ullah, "Comparative study of standalone and hybrid solar energy systems suitable for off-grid rural electrification: A review," *Renewable and Sustainable Energy Reviews*, vol. 27, pp. 738 – 752, 2013.

[8] A. J. McEvoy, L. Castañer, and T. Markvart, "Practical handbook of photovoltaics (second edition)." Boston: Academic Press, 2012.

[9] A. Merabet, V. Rajasekaran, A. McMullin, H. Ibrahim, R. Beguenane, and J. S. Thongam, "Nonlinear model predictive controller with state observer for speed sensorless

induction generator–wind turbine systems," in *Proceedings of the Institution of Mechanical Engineers, Part I: Journal of Systems and Control Engineering*, vol. *227*, no. 2 pp.198-213, Oct 2012.

[10] H. H. Aly and M. E. El-Hawary, "An overview of offshore wind electric energy resources," in *CCECE 2010*, May 2010, pp. 1–8.

[11] A. Merabet, J. Thongam, A. Safaee and M. Pahlevaninezhad, "Robust decoupling strategy for speed control of permanent magnet synchronous generator in wind energy conversion systems," *2011 IEEE International Electric Machines & Drives Conference (IEMDC)*, Niagara Falls, ON, 2011, pp. 1107-1112.

[12] A. A. Tanvir, A. Merabet, and R. Beguenane, "Real-time control of active and reactive power for doubly fed induction generator (DFIG)-based wind energy conversion system," *Energies*, vol. 8, no. 9, pp. 10389–10408, 2015.

[13] R. Harrison, E. Hau, and H. Snel, *Large Wind Turbines: Design and Economics*. John Wiley & Sons, 2001.

[14] F. Blaabjerg, Z. Chen, and S. B. Kjaer, "Power electronics as efficient interface in dispersed power generation systems," *IEEE Transactions on Power Electronics*, vol. 19, no. 5, pp. 1184–1194, Sept 2004.

[15] A. Merabet, M. A. Islam, R. Beguenane, A.M. Trzynadlowski, "Multivariable control algorithm for laboratory experiments in wind energy conversion", in *Renewable Energy*, vol. 83, no. 1, pp. 162-170, Apr. 2015.

[16] A. Merabet, M. A. Islam, R. Beguenane, H. Ibrahim (2014), “Second-order sliding mode control for variable speed wind turbine experiment system,” in *Renewable Energy & Power Quality Journal*, vol. 12, no. 12, pp. 1-6, Apr. 2014.

[17] T. Suzuki, H. Okitsu, and T. Kawahito, “Characteristics of a small wind power system with dc generator,” *IEE Proceedings B - Electric Power Applications*, vol. 129, no. 4, pp. 217–220, July 1982.

[18] K. A. Tawfique, A. Merabet, H. Ibrahim and R. Beguenane, "Standalone wind energy conversion system using OPAL-RT real-time HIL/RCP laboratory," 2016 International Conference on Industrial Informatics and Computer Systems (CIICS), Sharjah, 2016, pp. 1-5.

[19] H. Ibrahim, R. Beguenane and A. Merabet, "Technical and financial benefits of electrical energy storage," *2012 IEEE Electrical Power and Energy Conference*, London, ON, 2012, pp. 86-91.

[20] C. Ghenai, T. Salameh, A. Merabet and A. K. Hamid, "Modeling and optimization of hybrid solar-diesel-battery power system," *2017 7th International Conference on Modeling, Simulation, and Applied Optimization (ICMSAO)*, Sharjah, 2017, pp. 1-5.

[21] M. A. Green, *Power to the People: Sunlight to Electricity Using Solar Cells*. UNSW Press, 2000.

[22] A. Merabet, K. T. Ahmed, H. Ibrahim, R. Beguenane, and A. M. Y. M. Ghias, “Energy management and control system for laboratory scale microgrid based wind- PV-battery,” *IEEE Transactions on Sustainable Energy*, vol. 8, no. 1, pp. 145–154, Jan 2017.

[23] A. Merabet, K. A. Tawfique, M. A. Islam, S. Enebeli, and R. Beguenane, “Wind turbine emulator using Opal-RT real-time HIL/RCP laboratory,” in *2014 26th International Conference on Microelectronics (ICM)*, Dec 2014, pp. 192–195.

[24] S. Kouro, J. I. Leon, D. Vinnikov, and L. G. Franquelo, “Grid-connected photovoltaic systems: An overview of recent research and emerging PV converter technology,” *IEEE Industrial Electronics Magazine*, vol. 9, no. 1, pp. 47–61, March 2015.

[25] A. N. A. Ali, M. H. Saied, M. Z. Mostafa, and T. M. Abdel-Moneim, “A survey of maximum ppt techniques of PV systems,” in *2012 IEEE Energytech*, May 2012, pp. 1–17.

[26] B. Bendib, H. Belmili, and F. Krim, “A survey of the most used MPPT methods: Conventional and advanced algorithms applied for photovoltaic systems,” *Renewable and Sustainable Energy Reviews*, vol. 45, pp. 637 – 648, 2015.

[27] D. Verma, S. Nema, A. Shandilya, and S. K. Dash, “Maximum power point tracking (MPPT) techniques: Recapitulation in solar photovoltaic systems,” *Renewable and Sustainable Energy Reviews*, vol. 54, pp. 1018 – 1034, 2016.

[28] E. Koutroulis, K. Kalaitzakis, and N. C. Voulgaris, “Development of a microcontroller-based, photovoltaic maximum power point tracking control system,” *IEEE Transactions on Power Electronics*, vol. 16, no. 1, pp. 46–54, Jan 2001.

[29] Z. Almukhtar and A. Merabet, “Fuzzy MPPT Control and Power Regulation for Standalone Photovoltaic Energy Conversion System,” in *International Journal of Advanced Engineering Research and Applications (IJA-ERA)*, vol. 2, no. 7, pp. 371-381, Nov. 2016.

[30] Y.H. Liu, C.L. Liu, J.W. Huang, and J.H. Chen, “Neural-network-based maximum power point tracking methods for photovoltaic systems operating under fast changing environments,” *Solar Energy*, vol. 89, pp. 42 – 53, 2013.

[31] Z. Salam, J. Ahmed, and B. S. Merugu, “The application of soft computing methods for mppt of pv system: A technological and status review,” *Applied Energy*, vol. 107, pp. 135 – 148, 2013.

[32] F. Blaabjerg, R. Teodorescu, M. Liserre, and A. V. Timbus, “Overview of control and grid synchronization for distributed power generation systems,” *IEEE Transactions on Industrial Electronics*, vol. 53, no. 5, pp. 1398–1409, Oct 2006.

[33] A. Merabet, K. T. Ahmed, H. Ibrahim, R. Beguenane and K. Belmokhtar, "Sliding mode speed control for wind energy conversion systems," *2015 IEEE 28th Canadian Conference on Electrical and Computer Engineering (CCECE)*, Halifax, NS, 2015, pp. 1130-1134.

[34] R. Teodorescu, M. Liserre, and P. Rodríguez, *Grid Converters for Photovoltaic and Wind Power Systems*. United States: Wiley-IEEE Press, 2011.

[35] A. Merabet, L. Labib, and A. M. Y. M. Ghias, “Robust model predictive control for photovoltaic inverter system with grid fault ride-through capability.” *IEEE Transactions on Smart Grid*, vol. PP, no. 99, pp. 1–1, 2017.

[36] A. Timbus, M. Liserre, R. Teodorescu, P. Rodríguez, and F. Blaabjerg, “Evaluation of current controllers for distributed power generation systems,” *IEEE Transactions on Power Electronics*, vol. 24, no. 3, pp. 654–664, March 2009.

[37] S. A. Khajehoddin, M. Karimi-Ghartemani, A. Bakhshai, and P. Jain, “A power control method with simple structure and fast dynamic response for single-phase grid-connected DG systems,” *IEEE Transactions on Power Electronics*, vol. 28, no. 1, pp. 221–233, Jan 2013.

[38] A. G. Yepes, F. D. Freijedo, O. Lopez, and J. D. Gandoy, “Analysis and design of resonant current controllers for voltage-source converters by means of Nyquist diagrams and sensitivity function,” *IEEE Transactions on Industrial Electronics*, vol. 58, no. 11, pp. 5231–5250, Nov 2011.

[39] (2017) Gwec –Global Wind 2016 Report.[Online]. Available: http://www.gwec.net.

[40] A. Merabet, M. A. Islam, R. Beguenane, “Predictive speed controller for laboratory size wind turbine experiment system”, in *Canadian Conference on Electrical and Computer Engineering*, Toronto, ON, Canada, May 2014, pp. 1-6.

[41] A. Merabet, J. Thongam and J. Gu, “Torque and pitch angle control for variable speed wind turbines in all operating regimes,” *2011 10th International Conference on Environment and Electrical Engineering*, Rome, 2011, pp. 1-5.

[42] P. Rodríguez, A. V. Timbus, R. Teodorescu, M. Liserre, and F. Blaabjerg, “Flexible active power control of distributed power generation systems during grid faults,” *IEEE Transactions on Industrial Electronics*, vol. 54, no. 5, pp. 2583–2592, Oct 2007.

[43] F. Blaabjerg and K. Ma, “Future on power electronics for wind turbine systems,” *IEEE Journal of Emerging and Selected Topics in Power Electronics*, vol. 1, no. 3, pp. 139–152, Sept 2013.

[44] J. S. Thongam, M. Tarbouchi, R. Beguenane, A. F. Okou, A. Merabet, and P. Bouchard, “A Power Maximization Controller for PMSG Wind Energy Conversion Systems,” in *Journal of Electrical and Control Engineering*, vol. 3, no. 6, pp. 1-8, Sep. 2013.

[45] J. G. Slootweg, S. W. H. de Haan, H. Polinder, and W. L. Kling, “General model for representing variable speed wind turbines in power system dynamics simulations,” *IEEE Transactions on Power Systems*, vol. 18, no. 1, pp. 144–151, Feb 2003.

[46] Z. Chen, J. M. Guerrero, and F. Blaabjerg, “A review of the state of the art of power electronics for wind turbines,” *IEEE Transactions on Power Electronics*, vol. 24, no. 8, pp. 1859–1875, Aug 2009.

[47] A. Merabet, J. Thongam, A. Safaee and M. Pahlevaninezhad, "Robust decoupling strategy for speed control of permanent magnet synchronous generator in wind energy conversion systems," *2011 IEEE International Electric Machines & Drives Conference (IEMDC)*, Niagara Falls, ON, 2011, pp. 1107-1112.

[48] D. S. Oliveira Jr., M. M. Reis, C. E. A. Silva, L. H. S. Colado Barreto, F. L. M. Antunes and B. L. Soares, "A Three-Phase High-Frequency Semicontrolled Rectifier for PM WECS," in *IEEE Transactions on Power Electronics*, vol. 25, no. 3, pp. 677-685, March 2010.

[49] J. Dai, D. Xu, and B. Wu, “A novel control system for current source converter based variable speed pm wind power generators,” in *2007 IEEE Power Electronics Specialists Conference*, June 2007, pp. 1852–1857.

[50] J. S. Thongam, P. Bouchard, R. Beguenane, A. F. Okou and A. Merabet, "Control of variable speed wind energy conversion system using a wind speed sensorless optimum speed MPPT control method," *IECON 2011 - 37th Annual Conference of the IEEE Industrial Electronics Society*, Melbourne, VIC, 2011, pp. 855-860.

[51] A. Yazdani and R. Iravani, “A neutral-point clamped converter system for direct-drive variable-speed wind power unit,” *IEEE Transactions on Energy Conversion*, vol. 21, no. 2, pp. 596–607, June 2006.

[52] A. Merabet, K. T. Ahmed, H. Ibrahim and R. Beguenane, "Implementation of Sliding Mode Control System for Generator and Grid Sides Control of Wind Energy Conversion System," in *IEEE Transactions on Sustainable Energy*, vol. 7, no. 3, pp. 1327-1335, July 2016.

[53] J. Wang, D. Xu, B. Wu, and Z. Luo, “A low-cost rectifier topology for variable-speed high-power pmsg wind turbines,” *IEEE Transactions on Power Electronics*, vol. 26, no. 8, pp. 2192–2200, Aug 2011.

[54] (2017) Grid code high and extra high voltage. [Online]. Available: http://www.eon-netz.com.

[55] M. R. Islam and H. A. Gabbar, “Study of microgrid safety & protection strategies with control system infrastructures,” *Smart Grid and Renewable Energy*, vol. 3, no. 1, pp. 1–9, Nov 2011.

[56] *IEEE Standard for Interconnecting Distributed Resources with Electric Power Systems*. IEEE Standard 1547, 2003.

[57] F. Wang, J. L. Duarte, and M. A. M. Hendrix, “Pliant active and reactive power control for grid-interactive converters under unbalanced voltage dips,” *IEEE Transactions on Power Electronics*, vol. 26, no. 5, pp. 1511–1521, May 2011.

[58] A. Micallef, M. Apap, C. Spiteri-Staines, and J. M. Guerrero, “Single-phase microgrid with seamless transition capabilities between modes of operation,” *IEEE Transactions on Smart Grid*, vol. 6, no. 6, pp. 2736–2745, Nov 2015.

[59] H. C. Chen, C. T. Lee, P. T. Cheng, R. Teodorescu, and F. Blaabjerg, “A low-voltage ride-through technique for grid-connected converters with reduced power transistors stress,” *IEEE Transactions on Power Electronics*, vol. 31, no. 12, pp. 8562–8571, Dec 2016.

[60] A. Merabet, L. Labib, A. M. Y. M. Ghias, C. Ghenai, and T. Salameh, “Robust feedback linearizing control with sliding mode compensation for a grid-connected photovoltaic inverter system under unbalanced grid voltages,” *IEEE Journal of Photovoltaics*, vol. 7, no. 3, pp. 828–838, May 2017.

[61] (2017) Technical regulation 3.2.5 for wind power plants with a power output greater than 11 kw. [Online]. Available: http://www.energinet.dk

[62] R. Cárdenas, M. Díaz, F. Rojas, J. Clare and P. Wheeler, “Resonant control system for low-voltage ride-through in wind energy conversion systems,” *IET Power Electronics*, vol. 9, no. 6, pp. 1297–1305, 2016.

[63] F. Deng and Z. Chen, “Low-voltage ride-through of variable speed wind turbines with permanent magnet synchronous generator,” in *2009 35th Annual Conference of IEEE Industrial Electronics*, Nov 2009, pp. 621–626.

[64] M. Mirhosseini, J. Pou, B. Karanayil, and V. G. Agelidis, “Resonant versus conventional controllers in grid-connected photovoltaic power plants under unbalanced grid voltages,” *IEEE Transactions on Sustainable Energy*, vol. 7, no. 3, pp. 1124–1132, July 2016.

[65] P. Rodríguez, J. Pou, J. Bergas, J. I. Candela, R. P. Burgos, and D. Boroyevich, “Decoupled double synchronous reference frame pll for power converters control,” *IEEE Transactions on Power Electronics*, vol. 22, no. 2, pp. 584–592, March 2007.

[66] P. Rodríguez, A. Luna, R. S. Muñoz-Aguilar, I. Etxeberria-Otadui, R. Teodorescu and F. Blaabjerg, “A stationary reference frame grid synchronization system for three-phase grid-connected power converters under adverse grid conditions,” *IEEE Transactions on Power Electronics*, vol. 27, no. 1, pp. 99–112, Jan 2012.

[67] X. Guo, W. Wu, and Z. Chen, “Multiple-complex coefficient-filter-based phase-locked loop and synchronization technique for three-phase gridinterfaced converters in distributed utility networks,” *IEEE Transactions on Industrial Electronics*, vol. 58, no. 4, pp. 1194–1204, April 2011.

[68] J. Miret, M. Castilla, A. Camacho, L. G. d. Vicuña and J. Matas, “Control scheme for photovoltaic three-phase inverters to minimize peak currents during unbalanced grid-voltage sags,” *IEEE Transactions on Power Electronics*, vol. 27, no. 10, pp. 4262–4271, Oct 2012.

[69] V. Valouch, M. Bejvl, P. Šimek and J. Škramlík, "Power Control of Grid-Connected Converters Under Unbalanced Voltage Conditions," in *IEEE Transactions on Industrial Electronics*, vol. 62, no. 7, pp. 4241-4248, July 2015.

[70] S. F. Chou, C. T. Lee, H. C. Ko, and P. T. Cheng, “A low-voltage ride through method with transformer flux compensation capability of renewable power grid-side converters,” *IEEE Transactions on Power Electronics*, vol. 29, no. 4, pp. 1710–1719, April 2014.

[71] F. J. Lin, K. C. Lu, T. H. Ke, B. H. Yang, and Y. R. Chang, “Reactive power control of three-phase grid-connected pv system during grid faults using takagi–sugeno–kang probabilistic fuzzy neural network control,” *IEEE Transactions on Industrial Electronics*, vol. 62, no. 9, pp. 5516–5528, Sept 2015.

[72] “IEEE standard for interconnecting distributed resources with electric power systems,” *IEEE Std 1547-2003*, pp. 1–28, July 2003.

[73] *CanWEA–Canadian grid code for wind development review and recommendations*. Garrad Hassan Canada Inc., 2005.

[74] M. Tsili and S. Papathanassiou, “A review of grid code technical requirements for wind farms,” *IET Renewable Power Generation*, vol. 3, no. 3, pp. 308–332, Sept 2009.

[75] G. Clarke, D. Bailey, and F. Castro, *New generation Technologies and GB Grid Codes*. Sinclair Knight Merz, 2004.

[76] (2017) The UK Grid Code. [Online]. Available: http://www2.nationalgrid.com

[77] Y. Yang, W. Chen, and F. Blaabjerg, *Advanced Control of Photovoltaic and Wind Turbines Power Systems*. Springer International Publishing, 2014.

[78] Y. Xue, K. C. Divya, G. Griepentrog, M. Liviu, S. Suresh, and M. Manjrekar, "Towards next generation photovoltaic inverters," in *2011 IEEE Energy Conversion Congress and Exposition*, Sept 2011, pp. 2467–2474.

[79] M. A. Islam, A. Merabet, R. Beguenane, and H. Ibrahim, "Modeling solar photovoltaic cell and simulated performance analysis of a 250w PV module," in *2013 IEEE Electrical Power Energy Conference*, Aug 2013, pp. 1–6.

[80] M. A. Islam, A. Merabet, R. Beguenane, and H. Ibrahim, "Power management strategy for solar-wind-diesel stand-alone hybrid energy system," *International Journal of Electrical, Computer, Energetic, Electronic and Communication Engineering*, vol. 8, no. 6, pp. 843 – 847, 2014.

[81] M. G. Villalva, J. R. Gazoli, and E. R. Filho, "Comprehensive approach to modeling and simulation of photovoltaic arrays," *IEEE Transactions on Power Electronics*, vol. 24, no. 5, pp. 1198–1208, May 2009.

[82] A. Merabet, K. T. Ahmed, R. Beguenane, and H. Ibrahim, "Feedback linearization control with sliding mode disturbance compensator for PMSG based wind energy

conversion system," in *2015 IEEE 28th Canadian Conference on Electrical and Computer Engineering (CCECE)*, May 2015, pp. 943–947.

[83] Ahmed Said Khalifa, "Control and Interfacing of Three Phase Grid Connected Photovoltaic Systems, University of Waterloo, 2010.

[84] A. S. Khalifa and E. F. El-Saadany, "Control of three phase grid connected photovoltaic power systems," in *Proceedings of 14th International Conference on Harmonics and Quality of Power - ICHQP 2010*, Sept 2010, pp. 1–7.

[85] B. Wu, *High-Power Converters and AC Drives*. John Wiley & Sons, 2007.

[86] Z. Almukhtar and A. Merabet, " Maximum Power Point Tracking Based on Estimated Power for PV Energy Conversion System," in *International Journal of Electrical, Computer, Energetic, Electronic and Communication Engineering*, vol. 10, no. 4, pp. 573-577, June 2016.

[87] V. Salas, E. Olías, A. Barrado, and A. Lázaro, "Review of the maximum power point tracking algorithms for stand-alone photovoltaic systems," *Solar Energy Materials and Solar Cells*, vol. 90, no. 11, pp. 1555 – 1578, 2006.

[88] M. A. Islam, *Power Management and Control for Solar-Wind-Diesel Standalone Hybrid Energy Systems*. Saint Mary's University, 2013.

[89] K. T. Ahmed, A. Merabet, R. Beguenane, H. Ibrahim and A. Allagui, "Real-time platform for controlling DC microgrid based standalone solar energy conversion system," *2016 International Conference on Industrial Informatics and Computer Systems (CIICS)*, Sharjah, 2016, pp. 1-5.

[90] C. Xia, Q. Geng, X. Gu, T. Shi, and Z. Song, “Input-output feedback linearization and speed control of a surface permanent-magnet synchronous wind generator with the boost-chopper converter,” *IEEE Transactions on Industrial Electronics*, vol. 59, no. 9, pp. 3489–3500, Sept 2012.

[91] P. V. J. Belanger and J. N. Paquin, *The What, Where, and Why of Real Time Simulation*. OPAL-RT Publication, 2010.

[92] K. A. Tawfique, A. Merabet, H. Ibrahim and R. Beguenane, "Standalone wind energy conversion system using OPAL-RT real-time HIL/RCP laboratory," *2016 International Conference on Industrial Informatics and Computer Systems (CIICS)*, Sharjah, 2016, pp. 1-5.

[93] P. M. Menghal and A. J. Laxmi, “Real time simulation: A novel approach in engineering education,” in *2011 3rd International Conference on Electronics Computer Technology*, vol. 1, April 2011, pp. 215–219.

[94] (2017) Real-time simulation. [Online]. Available: http://www.opalrt.com/training-programs-overview/.

[95] K. Beddek, A. Merabet, M. Kesraoui, A. A. Tanvir and R. Beguenane, "Signal-Based Sensor Fault Detection and Isolation for PMSG in Wind Energy Conversion Systems," in *IEEE Transactions on Instrumentation and Measurement*, vol. 66, no. 9, pp. 2403-2412, Sept. 2017.

[96] A. Merabet, A. A. Tanvir and K. Beddek, "Torque and state estimation for real-time implementation of multivariable control in sensorless induction motor drives," in *IET Electric Power Applications*, vol. 11, no. 4, pp. 653-663, April 2017.